Dynamic Inversion Flight Control Laws for Automatic Transition of Tilt-Rotor/Wing Aircraft

Umberto Saetti*
Assistant Professor
Department of Aerospace Engineering, University of Maryland, College Park, MD

This article presents the development and demonstration of dynamic inversion (DI) flight control laws for the automatic transition of tilt-rotor/wing aircraft from hover to cruise flight. The DI control laws employ a multiloop architecture without requiring gain scheduling; however, feedback linearization must be scheduled based on the aircraft's linearized dynamics, which depend on variables such as airspeed and nacelle angle. A generic multirotor/wing simulation model is adapted to represent four configurations: a Bell XV-15-like tilt-rotor, two eVTOL aircraft resembling the Joby S4 and Archer Midnight, and a tilt-wing aircraft similar to the NASA Tilt Wing. The XV-15-like model is validated against US Army/NASA flight-test data and existing models. The simulation models are trimmed and linearized across speed increments from hover to cruise, and model-order reduction methods are applied for control design. The DI control laws are shown to comply with frequency-domain-based stability, performance, and handling quality specifications in selected flight conditions. Closed-loop simulations using the full-order nonlinear dynamics of all configurations demonstrate successful automatic transitions from hover to cruise with accurate forward speed tracking and minimal off-axis response.

Introduction

Future Vertical Lift (FVL) vehicles and electric vertical take-off and landing (eVTOL) vehicles intended for urban air mobility (UAM) feature multiple rotors, rigid rotor systems, and high levels of aerodynamic interactions which pose significant modeling, simulation, and control challenges. FVL configurations include winged single main rotor, lift-offset coaxial, and tilt-rotor configurations (Refs. 1–4). Attempts to categorize the various UAM eVTOL configurations are provided in Refs. 5 and 6. In these studies, configurations are differentiated between rotary-wing cruise and fixed-wing cruise. The rotary-wing cruise category includes rotary-wing and lift-fan aircraft, whereas the fixed-wing category includes lift+cruise, tilt-wing/rotor, and tailsitter aircraft. Tilt-rotor/wing configurations, which are the only common configuration between FVL and UAM, pose particular control challenges due to their hybrid design, which combines the features of both helicopters and fixed-wing aircraft. Key challenges include (i) the transition from vertical take-off and landing (VTOL) (or helicopter) mode and high-speed forward flight (or airplane) mode, characterized by the tilting motion of the rotors and/or wings tilt; (ii) significant differences in the stability and response characteristics between VTOL, high-speed forward flight, and transition modes; (iii) significant rotor-on-rotor and rotor-on-wing interactions that vary dramatically between operational modes and have similarly dramatic effects on the flight dynamics; (iv) the presence of redundant control surfaces, such that the control signal needs to be reallocated intelligently across the redundant control effectors; and (v) proneness to gust disturbances and therefore need flight control systems able to mitigate these deficiencies.

All of these control challenges require flexible, yet robust, control architectures to provide desired stability, response, and handling quality characteristics across the flight envelope. Moreover, it is important that the closed-loop dynamics yield a simple, predictable response to commanded output that is common across operational modes to minimize pilot workload. Conversion control laws for tilt-rotor/wing aircraft have been investigated in the past, with examples including optimal control (Refs. 7–9), total energy control system algorithm (Ref. 10), nonlinear time-varying control (Ref. 11), nonlinear optimal control (Ref. 12), nonlinear control based on Lyapunov theory (Ref. 13), active adaptive model inversion (Ref. 14), hybrid dynamic inversion (DI) and explicit model following (EMF) (Ref. 15), incremental nonlinear dynamic inversion (Ref. 16), as well as other methods (Refs. 17–19). While all of these studies achieved successful conversion of more or less sophisticated models of tilt-rotor/wing aircraft, only Refs. 15 and 19 focused on handling-quality evaluations. In fact, both DI and EMF are model-following control methods that are particularly suited for gust disturbance rejection and for stability, performance, and handling quality evaluations as specified in the MIL-DTL-32742 specifications for military rotorcraft (Ref. 20).

Model following control architectures such as DI and EMF are especially well-suited for providing gust disturbance rejection. This is because their 2-degree-of-freedom (DoF) structure, with separate feed forward and feedback paths, allows to tune the rotorcraft response to gusts independently from responses to outer guidance/navigation loops. In

*Corresponding author; email: saetti@umd.edu
Manuscript received September 2024; accepted May 2025.

contrast, in 1-DoF classic control methodologies, the responses to gusts and outer guidance/navigation loops cannot be independently tuned. A key aspect of both architectures is the reliance on model inversion to cancel the plant dynamics and track a desired reference model. EMF is essentially a linear design method that uses a simplified model inversion in the feed-forward path to follow the desired reference model, while feedback design is applied to the high-order linear plant models that are either identified from flight-test data or obtained from physics-based models via linearization schemes. Generally, both feed-forward inversion and feedback compensation need to be scheduled with the flight condition to account for variations in the flight dynamics. DI, on the other hand, consolidates the flight condition dependencies into the plant model used in its feedback linearization loop, thereby reducing the need for gain scheduling in the controller design. However, the plant model used for feedback linearization still needs to be scheduled with the flight condition to accurately represent the system dynamics. When the plant model is known at each flight condition, either from flight test or simulation, DI becomes particularly attractive from the control system designer's perspective due to its ability to simplify implementation and streamline control design efforts.

With regard to past work on DI for tilt-rotor conversion, Berger et al. (Ref. 15) only developed outer-velocity DI control loops, whereas the inner-attitude loop was based on EMF. Moreover, these control laws were not demonstrated for automatic transition, rather for piloted transition, and were only demonstrated for quasi-linear parameter-varying models (Ref. 21). Moreover, to the best knowledge of the author, no published pure dynamic inversion control application exists for tilt-wing aircraft that has demonstrated automatic transition.

As such, the objectives of the present investigation are twofold. The first objective is to develop a DI flight control framework that is broadly applicable to any tilt-rotor/wing aircraft configuration and that provides desired stability, performance, and handling quality characteristics at hover, in high-forward flight, and during conversion between the two. The second objective is to demonstrate said flight control laws for four different tilt-rotor configurations: a tilt-rotor aircraft similar to a Bell XV-15, two tilt-rotor eVTOL aircraft reminiscent of Joby S4 and Archer Midnight vehicles, respectively, and a tilt-wing aircraft similar to the NASA Tilt Wing.

The paper begins with an overview of the simulation model and its adaptation to four tilt-rotor/wing configurations. This is followed by a detailed mathematical description of the linearization, trim, and model-order reduction algorithms. DI control laws are then developed based on a multiloop architecture and parameterized with flight speed to enable automatic transition from hover to cruise flight. These control laws are demonstrated for the configurations through simulations involving the transition from hover to 160 kt forward flight. Final remarks summarize the findings of the study and identify directions for future development.

Simulation Models

Overview

Simulation models are based on an in-house MATLAB®/Simulink generic multirotor/wing flight dynamics and control code with the following characteristics:

1) The aircraft fuselage is modeled as a rigid body. Fuselage aerodynamic forces are calculated based on equivalent flat-plate frontal, lateral, and vertical areas (Ref. 22).

2) The user can specify any number of rotors and/or wings at arbitrary (and time-varying) orientations on the aircraft body.

3) Accuracy of the rotor aeromechanics is selectable, with modeling methods being as simple as static inflow and no blade flapping, or as complex as a dynamic inflow (Ref. 23) and flexible blades based on finite element methods. Rotor aerodynamics can also account for rotor-on-rotor interactions (Refs. 24–27).

4) Wings accuracy level is also selectable. The most complex model consists of lifting-line theory. Rotor-on-wing aerodynamics interactions are calculated based on the circulation at each wing element/panel using Biot–Savart and Heyson (Ref. 28).

5) The model is implemented in MATLAB® to ease the design and testing of flight control laws.

6) The model is integrated with a baseline control law based on DI (Refs. 29–31), featuring inner-attitude and outer-velocity control loops. Collective pitch control is implemented as part of the outer loop architecture.

Simulation models are developed for four different tilt-rotor/wing aircraft configurations: a tilt-rotor aircraft similar to a Bell XV-15 (Refs. 30, 32), two tilt-rotor eVTOL aircraft reminiscent of Joby S4 and Archer Midnight vehicles, respectively, and a tilt-wing aircraft similar to the NASA Tilt Wing (Refs. 33, 34). These aircraft models will be referred to as "TR" (tilt rotor), "TMR" (tilt multirotor), "TMR2" (tilt multirotor 2), and "TW" (tilt wing), respectively, hereafter. The geometry of these four tilt-rotor/wing vehicles is shown in trimmed flight at hover and high-speed forward flight in Fig. 1. Note that for illustration purposes, the TMR, TMR2, and TW models feature a scaled XV-15 fuselage. This is because it was not possible to reproduce the Joby S4, Archer Midnight, or NASA Tilt Wing fuselage based on publicly available data. The general characteristics of the four aircraft are reported in Tables 1–4. The TR properties are largely based on Ref. 32, whereas the TMR, TMR2, and TW mass properties are scaled from those of the XV-15 based on relative mass and dimensions. Additionally, the TMR and TMR2 geometry parameters were estimated from publicly available pictures/drawings found online, whereas those of the NASA Tilt Wing were approximated from Refs. 33 and 34.

Nonlinear dynamics

The rotorcraft flight dynamics are formulated as a nonlinear time-periodic system:

$$\dot{\boldsymbol{x}} = \boldsymbol{f}(\boldsymbol{x}, \boldsymbol{u}, t) \tag{1a}$$

$$\boldsymbol{y} = \boldsymbol{g}(\boldsymbol{x}, \boldsymbol{u}, t) \tag{1b}$$

where $\boldsymbol{x} \in \mathbb{R}^n$ is the state vector, $\boldsymbol{u} \in \mathbb{R}^m$ is the control input vector, $\boldsymbol{y} \in \mathbb{R}^l$ is the output vector, and t is the dimensional time in seconds. It is convenient to note that dimensional time can be related to the azimuth angle ψ of a reference blade, also known as nondimensional time, via the following relation: $\psi = \Omega t$, where Ω is the angular speed, in rad/s, of the slowest rotor. It follows that the fundamental period of the system is $T = (2\pi)/\Omega$ seconds, which corresponds to 2π radians or one revolution of the slowest rotor. The nonlinear functions $\boldsymbol{f}$ and $\boldsymbol{g}$ are T-periodic in time such that

$$\boldsymbol{f}(\boldsymbol{x}, \boldsymbol{u}, t) = \boldsymbol{f}(\boldsymbol{x}, \boldsymbol{u}, t + T) \tag{2a}$$

$$\boldsymbol{g}(\boldsymbol{x}, \boldsymbol{u}, t) = \boldsymbol{g}(\boldsymbol{x}, \boldsymbol{u}, t + T) \tag{2b}$$

The state vector is

$$\boldsymbol{x}^T = \left[\boldsymbol{x}_{\mathrm{RB}}^T \; \boldsymbol{x}_{\mathrm{R}_1}^T \; \cdots \; \boldsymbol{x}_{\mathrm{R}_N}^T\right] \tag{3}$$

where $\boldsymbol{x}_{\mathrm{RB}}$ are the rigid-body states and $\boldsymbol{x}_{\mathrm{R}_i}$ are the states of the ith of N rotors. The rigid-body state vector is common to all aircraft and is given by

$$\boldsymbol{x}_{\mathrm{RB}}^T = [u \; v \; w \; p \; q \; r \; \phi \; \theta \; \psi \; x \; y \; z] \tag{4}$$

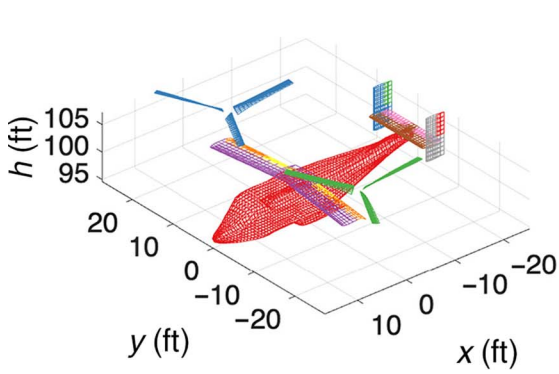

(a) TR at hover

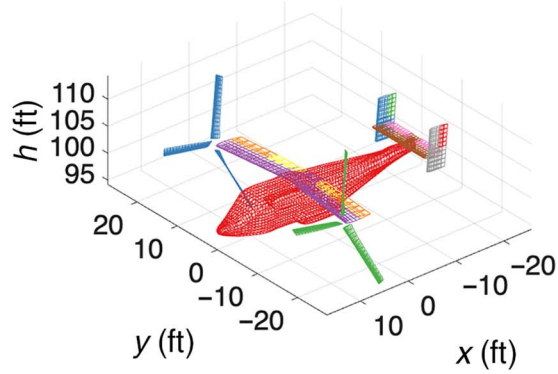

(b) TR in cruise flight

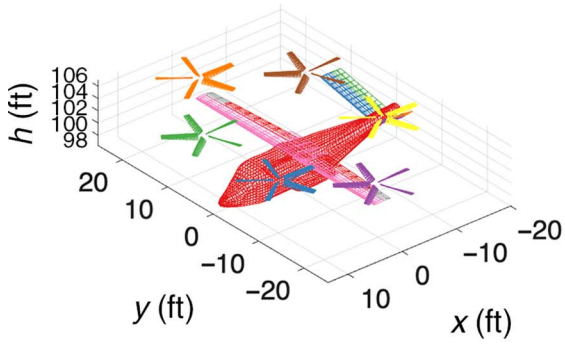

(c) TMR at hover

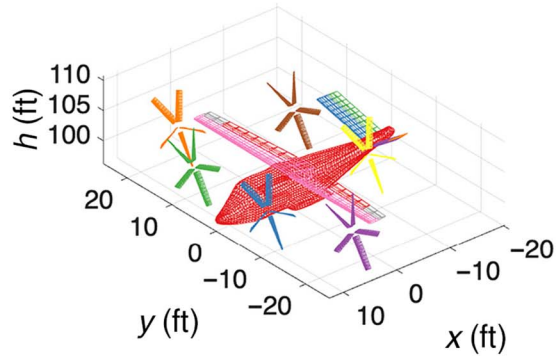

(d) TMR in cruise flight

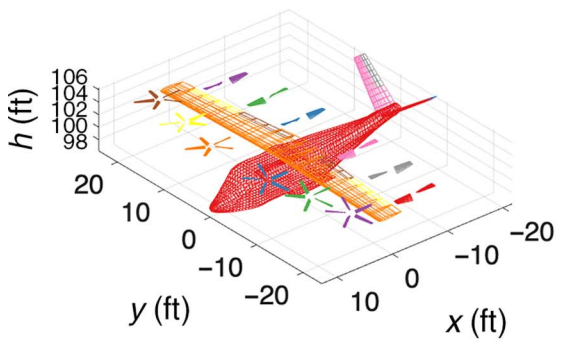

(e) TMR2 at hover

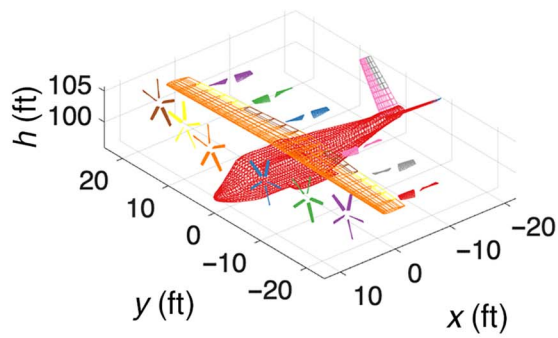

(f) TMR2 in cruise flight

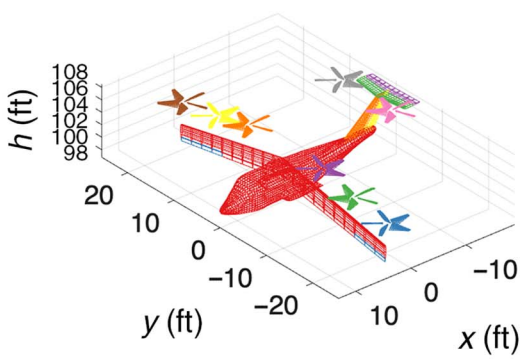

(g) TW at hover

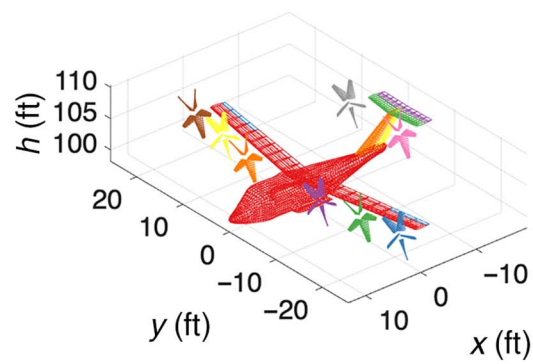

(h) TW in cruise flight

Fig. 1. Tilt-rotor/wing aircraft geometry at hover and cruise flight.

Table 1. General characteristics of the TR model (Ref. 32)

Parameter	Value	Units
Mass and inertia		
Gross weight, W	13000	lb
Roll-axis moment of inertia, I_{xx}	52795	sl-ft^2
Pitch-axis moment of inertia, I_{yy}	21360	sl-ft^2
Yaw-axis moment of inertia, I_{zz}	66335	sl-ft^2
Roll/yaw-axes product of inertia, I_0xz	1234	sl-ft^2
CG fuselage station	25	ft
CG butt line	0	ft
CG water line	6.8	ft
Fuselage		
Frontal drag area	23.11	ft^2
Sideward drag area	131.83	ft^2
Vertical drag area	184.11	ft^2
Fuselage station (center of pressure)	24.42	ft
Butt line (center of pressure)	0	ft
Water line (center of pressure)	5.42	ft
Rotors		
Number of blades	3	–
Radius	12.5	ft
Mean blade chord	1.19	ft
Blade twist	−40.9	deg
Blade weight	213.14	lb
Blade flapping inertia	102.5	sl-ft^2
Hub flapping spring	225	(sl-ft)/deg
Angular speed	61.68	rad/s
Shaft length	4.67	ft
Fuselage station (shaft pivot point)	25	ft
Butt line (shaft pivot point)	±16.08	ft
Water line (shaft pivot point)	8.33	ft
Wing		
Span	32.17	ft
Mean chord	5.26	ft
Twist	−3	deg
Sweep	−6.5	deg
Fuselage station (aerodynamic center)	24.31	ft
Butt line (aerodynamic center)	0	ft
Water line (aerodynamic center)	7.99	ft
Horizontal stabilizer		
Span	20	ft
Mean chord	3.92	ft
Fuselage station (aerodynamic center)	46.67	ft
Butt line (aerodynamic center)	0	ft
Water line (aerodynamic center)	8.58	ft
Vertical stabilizers		
Span	7.68	ft
Mean chord	3.73	ft
Fuselage station (aerodynamic center)	47.5	ft
Butt line (aerodynamic center)	±6.41	ft
Water line (aerodynamic center)	9.64	ft

Table 2. General characteristics of the TMR model

Parameter	Value	Units
Mass and inertia		
Gross weight, W	4800	lb
Roll-axis moment of inertia, I_{xx}	28650	sl-ft^2
Pitch-axis moment of inertia, I_{yy}	1962	sl-ft^2
Yaw-axis moment of inertia, I_{zz}	17118	sl-ft^2
Roll/yaw-axes product of inertia, I_{xz}	0	sl-ft^2
CG fuselage station	10.2	ft
CG butt line	0	ft
CG water line	3.86	ft
Fuselage		
Frontal drag area	26.69	ft^2
Sideward drag area	135.08	ft^2
Vertical drag area	135.08	ft^2
Fuselage station (center of pressure)	10.15	ft
Butt line (center of pressure)	0	ft
Water line (center of pressure)	2.66	ft
Rotors		
Number of blades	5	–
Radius	6.04	ft
Mean blade chord	0.9	ft
Blade twist	−30	deg
Shaft length	{1.65, 3.58, 1.93}	ft
Fuselage station (shaft pivot point)	{1.77, 10.2, 20.77}	ft
Butt line (shaft pivot point)	{±8.29, ±19.5, ±8.29}	ft
Water line (shaft pivot point)	{5.89, 5.23, 8.8}	ft
Wing		
Span	39	ft
Mean chord	4.11	ft
Twist	0	deg
Sweep	−2	deg
Fuselage station (aerodynamic center)	10.77	ft
Butt line (aerodynamic center)	0	ft
Water line (aerodynamic center)	5.5	ft
V-Tail		
Span	16.08	ft
Mean chord	3.8	ft
Twist	0	deg
Sweep	−20	deg
Dihedral	−35	deg
Fuselage station (aerodynamic center)	27.55	ft
Butt line (aerodynamic center)	0	ft
Water line (aerodynamic center)	5.5	ft

where u, v, w are the longitudinal, lateral, and vertical velocities in the body-fixed frame, p, q, r are the roll, pitch, and yaw rates, ϕ, θ, ψ are the Euler angles, and x, y, z are the positions in the north-east-down (NED) frame.

The general form of the ith rotor state vector is

$$\boldsymbol{x}_{\mathrm{R}_i}^T = \left[\boldsymbol{\beta}_{\mathrm{M}}^T \; \dot{\boldsymbol{\beta}}_{\mathrm{M}}^T \; \boldsymbol{\lambda}^T \; \Omega \; \psi_{\mathrm{R}}\right] \tag{5}$$

where $\boldsymbol{\beta}_{\mathrm{M}}$ is the flapping angles in multiblade coordinated, $\boldsymbol{\lambda}^T = [\lambda_0 \; \lambda_{1c} \; \lambda_{1s}]$ is a vector containing the dynamic inflow components, Ω is the rotor angular speed, and ψ_{R} is the azimuth angle of a reference blade.

It is worth noting that the state vector differs between the four aircraft models as the TRM, TMR2, and TW configurations do not feature blade flapping. Because the rotors are considered to be rigid, the flapping states are removed from the TMR, TMR2, and TW configuration state vectors.

The pilot input vector is

$$\boldsymbol{u}^T = [\delta_{\mathrm{lat}} \; \delta_{\mathrm{lon}} \; \delta_{\mathrm{col}} \; \delta_{\mathrm{ped}} \; \delta_{\mathrm{aux}}] \tag{6}$$

where δ_{lat} is the lateral and longitudinal stick position, δ_{lat} and δ_{lon} is the longitudinal stick position, δ_{col} is the collective stick position, δ_{ped} is the pedals position, and δ_{aux} is an auxiliary input that controls the rotor/wing tilt angle.

The pilot inputs are converted to actuator inputs via a mixing matrices scheduled with the aircraft absolute speed. Note that, in this study, the TR model does not adopt the control mixing relations in Ref. 32. The control

Table 3. General characteristics of the TMR2 model

Parameter	Value	Units
Mass and inertia		
Gross weight, W	6500	lb
Roll-axis moment of inertia, I_{xx}	56345	sl-ft^2
Pitch-axis moment of inertia, I_{yy}	63725	sl-ft^2
Yaw-axis moment of inertia, I_{zz}	38593	sl-ft^2
Roll/yaw-axes product of inertia, I_{xz}	0	sl-ft^2
CG fuselage station	10	ft
CG butt line	0	ft
CG water line	5.9	ft
Fuselage		
Frontal drag area	19.96	ft^2
Sideward drag area	123.81	ft^2
Vertical drag area	92.59	ft^2
Fuselage station (center of pressure)	10.15	ft
Butt line (center of pressure)	0	ft
Water line (center of pressure)	4.66	ft
Rotors		
Number of blades	{5, 2}	–
Radius	3.56	ft
Mean blade cord	{0.3920, 0.89}	ft
Blade twist	−40	deg
Shaft length	{1.4, 0}	ft
Fuselage station (shaft pivot point)	{2.45, 4.05, 5.40, 18.96, 17.12, 18.96}	ft
Butt line (shaft pivot point)	{±5.89, ±13.25, ±20.37}	ft
Water line (shaft pivot point)	7.53	ft
Wing		
Span	47	ft
Mean chord	5	ft
Twist	0	deg
Sweep	−4	deg
Fuselage station (aerodynamic center)	10.15	ft
Butt line (aerodynamic center)	0	ft
Water line (aerodynamic center)	7.9	ft
V-tail		
Span	8.85	ft
Mean chord	2.81	ft
Twist	0	deg
Sweep	2	deg
Dihedral	−35	deg
Fuselage station (aerodynamic center)	29.57	ft
Butt line (aerodynamic center)	0	ft
Water line (aerodynamic center)	9.59	ft

effector inputs are

$$\boldsymbol{u}_{\mathrm{C}}^{T} = \left[\boldsymbol{u}_{\mathrm{R}}^{T}\ \boldsymbol{u}_{\mathrm{W}}^{T}\right] \tag{7}$$

where $\boldsymbol{u}_{\mathrm{R}}$ are the rotor actuator inputs and $\boldsymbol{u}_{\mathrm{W}}$ are the wing actuator inputs. The actuator inputs for the ith rotor are

$$\boldsymbol{u}_{\mathrm{R}_i}^{T} = [\theta_0\ \theta_{1c}\ \theta_{1s}\ \Omega_{\mathrm{cmd}}\ \beta_{\mathrm{R}}] \tag{8}$$

where $\theta_0\ \theta_{1s}\ \theta_{1c}$ are the collective, longitudinal cyclic, and lateral cyclic swashplate inputs, Ω_{cmd} is the commanded rotor speed, and β_{R} is the rotor tilt angle.

It is also worth noting that the TMR and TW rotors are assumed to be pitch-only controlled and their angular speed to be prescribed with speed. On the other hand, the TMR2 rotors are assumed to be revolutions-per-minute (RPM) controlled, with blade pitch also prescribed with flight speed. The actuator inputs for the ith wing are

$$\boldsymbol{u}_{\mathrm{W}_i}^{T} = \left[\beta_{\mathrm{W}}\ \delta_{\mathrm{TE}}\ \cdots\ \delta_{\mathrm{TE}_N}\right] \tag{9}$$

where β_{W_i} is the wing tilt angle and δ_{TE_j} is the deflection of the jth trailing edge.

Trim, linearization, and model-order reduction

Linearized, time-invariant models are obtained by trimming the rotorcraft flight dynamics at desired flight conditions via the periodic trim algorithm of Refs. 30 and 35. Subsequently, the rotorcraft flight dynamics are linearized about each trim point via perturbation methods by only retaining the averaged (or zeroth) dynamics. To eliminate the need to measure or estimate states associated with the higher order dynamics, where the higher order dynamics include rotor and higher harmonic dynamics, it is desirable to reduce the order

Table 4. General characteristics of the TW model

Parameter	Value	Units
Mass and inertia		
Gross weight, W	6000	lb
Roll-axis moment of inertia, I_{xx}	28935	sl-ft^2
Pitch-axis moment of inertia, I_{yy}	5286	sl-ft^2
Yaw-axis moment of inertia, I_{zz}	25861	sl-ft^2
Roll/yaw-axes product of inertia, I_{xz}	0	sl-ft^2
CG fuselage station	8.7	ft
CG butt line	0	ft
CG water line	3.6	ft
Fuselage		
Frontal drag area	21.00	ft^2
Sideward drag area	101.51	ft^2
Vertical drag area	101.51	ft^2
Fuselage station (center of pressure)	9.7	ft
Butt line (center of pressure)	0	ft
Water line (center of pressure)	3.6	ft
Rotors		
Number of blades	5	–
Radius	3.67	ft
Mean blade chord	0.854	ft
Blade twist	−35	deg
Shaft length	{0.0, 1.01, 2.58, 0.9}	ft
Fuselage station (shaft pivot point)	{8.5, 8.5, 8.5, 23.14}	ft
Butt line (shaft pivot point)	{±22, ±14.78, ±7.91, ±5.47}	ft
Water line (shaft pivot point)	{6.474, 6.474, 6.474, 11}	ft
Wing		
Span	44	ft
Mean chord	3.08	ft
Twist	0	deg
Sweep	10	deg
Fuselage station (aerodynamic center)	8.03	ft
Butt line (aerodynamic center)	0	ft
Water line (aerodynamic center)	6.474	ft
Horizontal stabilizer		
Span	10.2	ft
Mean chord	3.2	ft
Twist	0	deg
Sweep	5	deg
Fuselage station (aerodynamic center)	25.72	ft
Butt line (aerodynamic center)	0	ft
Water line (aerodynamic center)	11	ft
Vertical stabilizer		
Span	5.28	ft
Mean chord	3.95	ft
Twist	0	deg
Sweep	30	deg
Fuselage station (aerodynamic center)	21.45	ft
Butt line (aerodynamic center)	0	ft
Water line (aerodynamic center)	8.5	ft

of the linearized dynamics. This is a necessary step to make linearized models tractable for practical control design purposes. This can be achieved through residualization, a portion of singular perturbation theory that pertains to Linear Time Invariant (LTI) systems (Ref. 36). Application of residualization to the rotorcraft flight dynamics can be found in several published research studies, for example, Refs. 29, 30, and 37–40.

Residualization begins with the assumption that one or more states have stable dynamics that are faster than that of the remaining states. Then, the state vector in Eq. (3) is partitioned into slow and fast components:

$$\boldsymbol{x}^T = \left[\boldsymbol{x}_\mathrm{s}^T \; \boldsymbol{x}_\mathrm{f}^T\right] \tag{10}$$

Then, the linearized dynamics can be re-written as

$$\begin{bmatrix}\dot{\boldsymbol{x}}_\mathrm{s}\\ \dot{\boldsymbol{x}}_\mathrm{f}\end{bmatrix} = \begin{bmatrix}\boldsymbol{A}_\mathrm{s} & \boldsymbol{A}_\mathrm{sf}\\ \boldsymbol{A}_\mathrm{fs} & \boldsymbol{A}_\mathrm{f}\end{bmatrix}\begin{bmatrix}\boldsymbol{x}_\mathrm{s}\\ \boldsymbol{x}_\mathrm{f}\end{bmatrix} + \begin{bmatrix}\boldsymbol{B}_\mathrm{s}\\ \boldsymbol{B}_\mathrm{f}\end{bmatrix}\boldsymbol{u} \tag{11}$$

By neglecting the dynamics of the fast states (i.e., $\dot{\boldsymbol{x}}_\mathrm{f} = 0$) and performing a few algebraic manipulations, the equations for a reduced-order system with the state vector composed of the slow states may be found:

$$\dot{\boldsymbol{x}}_\mathrm{s} = \hat{\boldsymbol{A}}\boldsymbol{x}_\mathrm{s} + \hat{\boldsymbol{B}}\boldsymbol{u} \tag{12}$$

where

$$\hat{\boldsymbol{A}} = \boldsymbol{A}_\mathrm{s} - \boldsymbol{A}_\mathrm{sf}\boldsymbol{A}_\mathrm{f}^{-1}\boldsymbol{A}_\mathrm{fs} \tag{13a}$$

$$\hat{\boldsymbol{B}} = \boldsymbol{B}_\mathrm{s} - \boldsymbol{A}_\mathrm{sf}\boldsymbol{A}_\mathrm{f}^{-1}\boldsymbol{B}_\mathrm{f} \tag{13b}$$

Note that $\boldsymbol{A}_\mathrm{f}$ must be invertible. This is guaranteed if $\boldsymbol{A}_\mathrm{f}$ is asymptotically stable, that is, all eigenvalues have their real part that is strictly negative. This condition is satisfied by choosing the rotor dynamics as the fast dynamics since the rotor dynamics are typically stable with eigenvalues on the far left of the complex plane. The slow states, on the other hand, are chosen as the rigid-body states with the exception of the position and heading states which are truncated as the rotorcraft dynamics are invariant with respect to these states (Ref. 41):

$$\boldsymbol{x}_\mathrm{s} = \boldsymbol{x}_\mathrm{RB} \tag{14a}$$

$$\boldsymbol{x}_\mathrm{f}^T = \left[\boldsymbol{x}_{\mathrm{R}_1}^T \; \boldsymbol{x}_{\mathrm{R}_2}^T\right] \tag{14b}$$

This way, an 8-state residualized system is obtained that still accounts for the higher order dynamics. A similar procedure is applied to the output equations of the linearized dynamics, which are reformulated as

$$\boldsymbol{y} = \left[\boldsymbol{C}_\mathrm{s} \; \boldsymbol{C}_\mathrm{f}\right]\begin{bmatrix}\boldsymbol{x}_\mathrm{s}\\ \boldsymbol{x}_\mathrm{f}\end{bmatrix} + \boldsymbol{D}\boldsymbol{u} \tag{15}$$

Then, it can be shown that the residualized output equations are

$$\boldsymbol{Y} = \hat{\boldsymbol{C}}\boldsymbol{x}_\mathrm{s} + \hat{\boldsymbol{D}}\boldsymbol{u} \tag{16}$$

where:

$$\hat{\boldsymbol{C}} = \boldsymbol{C}_\mathrm{s} - \boldsymbol{C}_\mathrm{f}\boldsymbol{A}_\mathrm{f}^{-1}\boldsymbol{A}_\mathrm{fs} \tag{17a}$$

$$\hat{\boldsymbol{D}} = \boldsymbol{D} - \boldsymbol{C}_\mathrm{f}\boldsymbol{A}_\mathrm{f}^{-1}\boldsymbol{B}_\mathrm{f} \tag{17b}$$

These reduced-order output equations capture the influence of the residualized dynamics on the output of the system.

Flight Control Design

General architecture

The flight control architecture chosen for this study is NDI. Application of NDI control laws to rotorcraft can be found in Refs. 15, 26, 30, 31, 37, 39, 40, and 42–48. A key aspect of DI is the reliance on model inversion to cancel the plant dynamics and track a desired reference model. One convenient feature of NDI is that it inverts the plant model within its feedback linearization loop. Compared to other conventional model-following control strategies, such as EMF, this approach reduces the explicit need for gain scheduling of the outer-loop control laws. However, the plant model used for feedback linearization still requires scheduling with the flight condition, as variations in aircraft dynamics must be accounted for. Additionally, the feedback gains may need to be scheduled in cases where consistent disturbance rejection (measured in disturbance

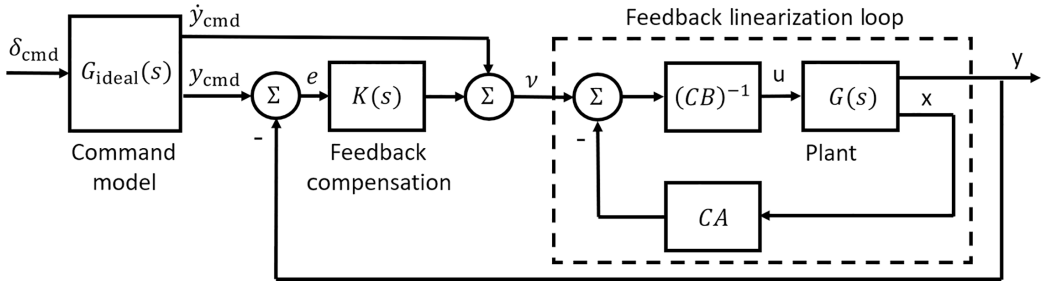

Fig. 2. DI controller as applied to a linear system.

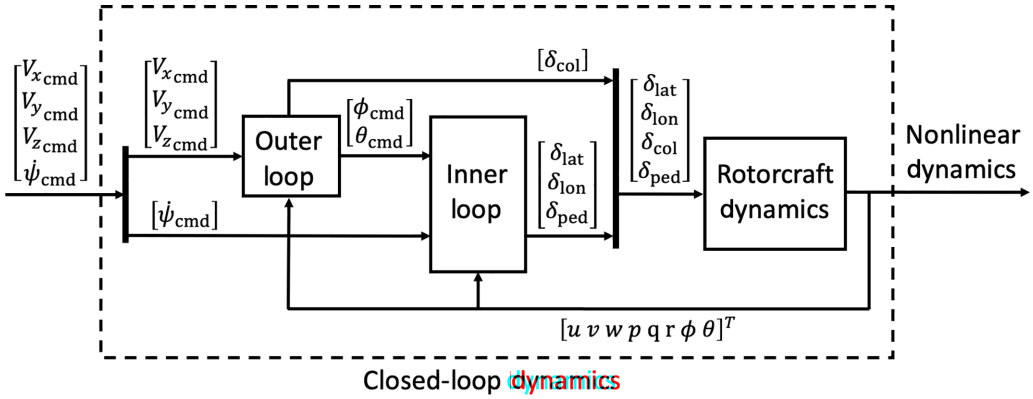

Fig. 3. Schematic of the closed-loop tilt-rotor/wing dynamics.

rejection bandwidth) and robustness performance (measured in broken-loop crossover frequency) must be maintained across the flight envelope. A generic DI controller as applied to a linear system is shown in Fig. 2. The key components include a command model (also referred to as a command filter or reference model) that specifies the desired response to pilot commands, a feedback compensation loop that minimizes tracking error, and an inner feedback loop that performs model inversion. (i.e., the feedback linearization loop).

A multiloop NDI control law based on Refs. 15, 26, 29, 30, and 42 is designed to enable automatic flight in low-speed flight (helicopter mode), cruise flight (airplane mode), and transition between the two. The schematic of the closed-loop rotorcraft dynamics is shown in Fig. 3. The outer loop controller, shown in Fig. 4(b) tracks longitudinal, lateral, and vertical ground velocities commands in the heading frame and calculates the desired pitch and roll attitudes for the inner loop to track, in addition to the collective control input setting. The desired response type for the outer loop is the translational rate command. The inner loop, shown in Fig. 4(a) achieves stability, disturbance rejection, and desired response characteristics about the roll, pitch, yaw, and heave axes. When coupled with the outer loop, an attitude command/attitude hold response is used for the roll and pitch axes, whereas a rate command/direction hold is used for the yaw axis.

Inner-attitude loop

The modified state vector used for the inner-attitude loop design is

$$\boldsymbol{x}^T = [p\ q\ r\ \phi\ \theta] \tag{18}$$

The system and control matrices of the corresponding modified system (i.e., $\boldsymbol{A}$ and $\boldsymbol{B}$) are obtained by truncating the rows and columns corresponding with the body-axes linear velocity states. Note that the stability and control derivatives are a function of the total speed $V = \sqrt{u^2 + v^2 + w^2}$. The controlled variables are the roll and pitch attitudes, along with the time derivative of the heading angle (i.e., the turn rate):

$$\boldsymbol{y}^T = [\phi\ \theta\ \dot{\psi}] \tag{19}$$

The output matrix that relates the state vector to the output vector:

$$\boldsymbol{C}^T = [\boldsymbol{C}_1^T\ \boldsymbol{C}_2^T] \tag{20}$$

where

$$\boldsymbol{C}_1 = \begin{bmatrix} 0\ 0\ 0\ 1\ 0 \\ 0\ 0\ 0\ 0\ 1 \end{bmatrix} \tag{21a}$$

$$\boldsymbol{C}_2 = [0\ 0\ 1\ 0\ 0] \tag{21b}$$

In the equation above, $\boldsymbol{C}_1$ corresponds to the roll and pitch attitudes whereas $\boldsymbol{C}_2$ corresponds to the yaw rate. This partitioning is due to the fact that the output equations for ϕ and θ must be differentiated twice to have the control inputs appear explicitly in the output equation, while the same procedure requires being performed once for the turn rate $\dot{\psi} \approx r$:

$$\begin{bmatrix} \ddot{\phi} \\ \ddot{\theta} \\ \dot{\psi} \end{bmatrix} = \begin{bmatrix} \boldsymbol{C}_1\boldsymbol{A}^2\boldsymbol{x} + \boldsymbol{C}_1\boldsymbol{A}\boldsymbol{B}\boldsymbol{u} \\ \boldsymbol{C}_2\boldsymbol{A}\boldsymbol{x} + \boldsymbol{C}_2\hat{\boldsymbol{B}}\boldsymbol{u} \end{bmatrix} \tag{22}$$

The objective of the DI control law is that the output $\boldsymbol{y}$ tracks a reference trajectory $\boldsymbol{y}_{\text{cmd}}(t)$ given by

$$\boldsymbol{y}_{\text{cmd}}^T = [\phi_{\text{cmd}}\ \theta_{\text{cmd}}\ \dot{\psi}_{\text{cmd}}] \tag{23}$$

with desired response characteristics. For this reason, the reference trajectory is fed through first- or second-order command models which dictate the desired response of the system. More specifically, ϕ_{cmd} and θ_{cmd} are fed through a second-order system, whereas r_{cmd} is fed through a first-order system. The command models are also used to extract the first and second derivatives of the filtered reference trajectory for use in the proportional-integral (PI) and proportional-integral-derivative (PID)

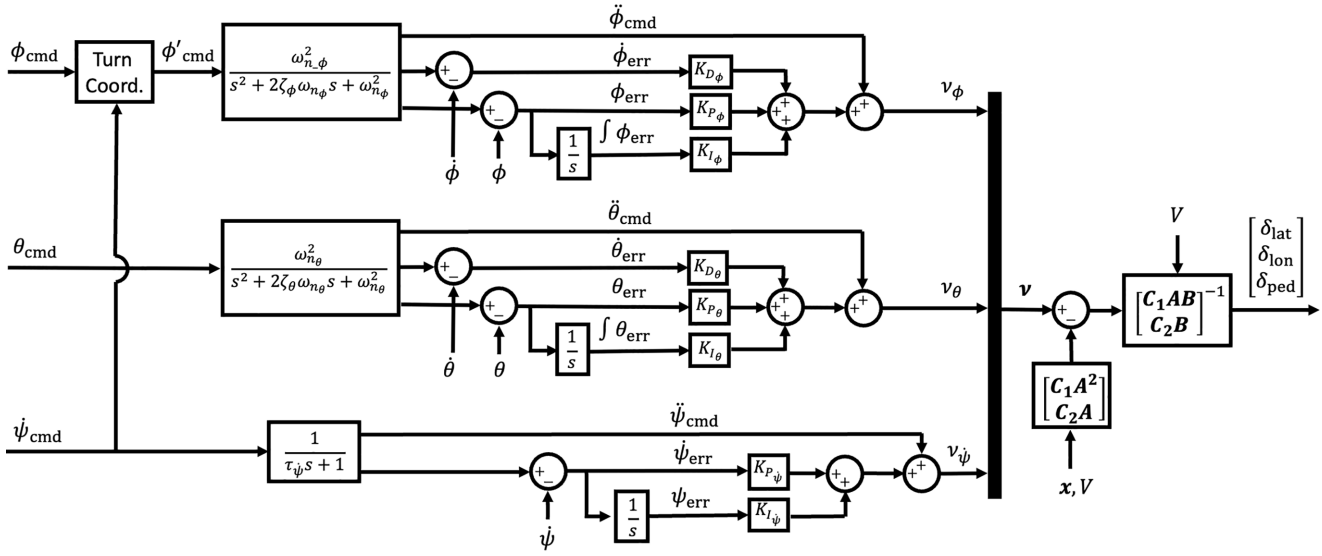

(a) Inner-attitude control loop

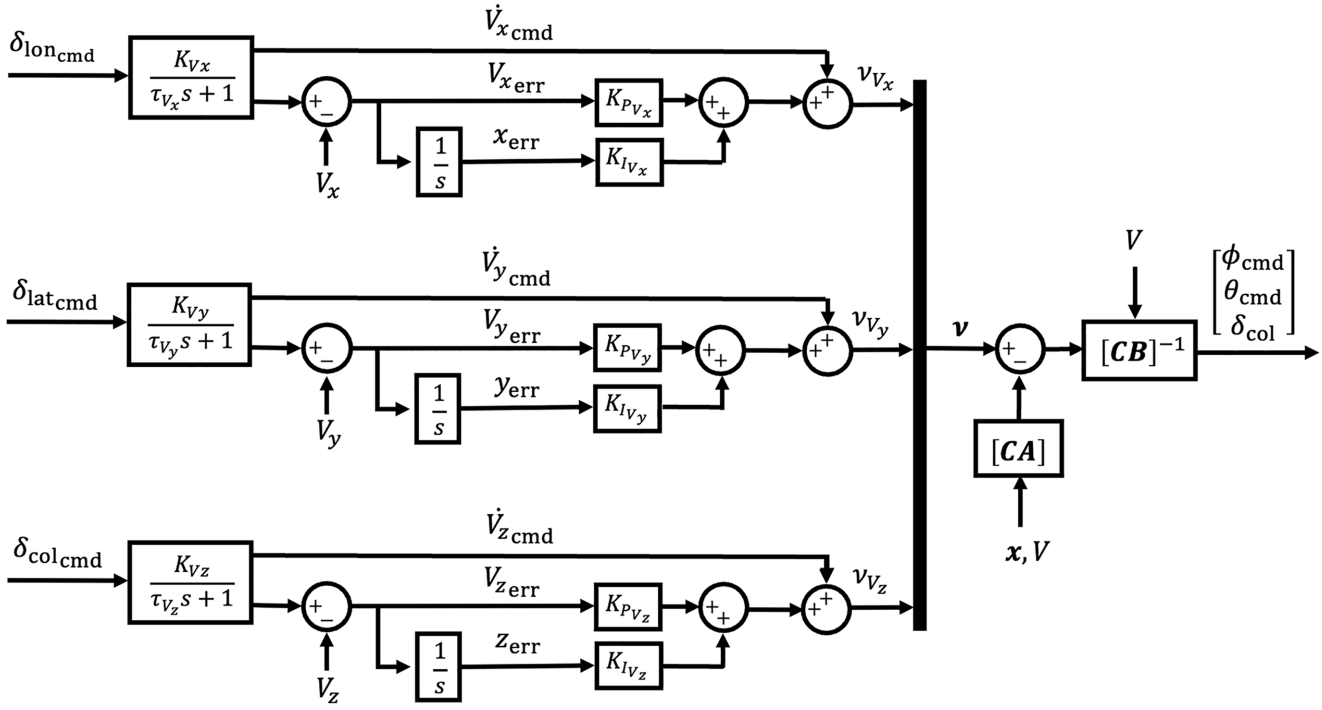

(b) Outer-velocity control loop

Fig. 4. Dynamic inversion inner-attitude and outer-velocity control loops.

compensators described below. The command models are of the following form:

$$G_{\text{ideal}}^{(1)}(s) = \frac{1}{\tau s + 1} \tag{24a}$$

$$G_{\text{ideal}}^{(2)}(s) = \frac{\omega_n^2}{s^2 + 2\omega_n\zeta + \omega_n^2} \tag{24b}$$

where τ is the first-order command model time constant, which is the inverse of the command model break frequency (i.e., $\tau = 1/\omega_n$). Additionally, ω_n and ζ are, respectively, the natural frequency and damping ratio of the second-order command model. PI and PID compensation are used to reject external disturbances and to compensate for discrepancies between the approximate model used in this derivation and the actual bare-airframe dynamics of the aircraft. The resulting DI control law is found by solving for the control vector in Eq. (22), leading to

$$\boldsymbol{u} = \begin{bmatrix}\boldsymbol{C}_1\boldsymbol{AB}\\ \boldsymbol{C}_2\boldsymbol{B}\end{bmatrix}^{-1}\left(\boldsymbol{\nu} - \begin{bmatrix}\boldsymbol{C}_1\boldsymbol{A}^2\\ \boldsymbol{C}_2\boldsymbol{A}\end{bmatrix}\boldsymbol{x}\right) \tag{25}$$

Table 5. Inner loop command models parameters

Command	ω_n (rad/s)	ζ
Roll attitude	4.0	0.7
Pitch attitude	3.5	0.7
Turn rate	2	–

Table 6. Outer loop command models properties

	τ (s)
$V_{x_{\text{cmd}}}$	0.5
$V_{y_{\text{cmd}}}$	0.5
$V_{z_{\text{cmd}}}$	0.5

where $\boldsymbol{\nu}$ is the pseudo-command vector and $\boldsymbol{e}$ is the error as defined in Eqs. (26) and (27), respectively.

$$\begin{bmatrix}\nu_\phi\\ \nu_\theta\\ \nu_{\dot\psi}\end{bmatrix}=\begin{bmatrix}\ddot\phi_{\text{cmd}}\\ \ddot\theta_{\text{cmd}}\\ \ddot\psi_{\text{cmd}}\end{bmatrix}+\boldsymbol{K}_P\begin{bmatrix}e_\phi\\ e_\theta\\ e_{\dot\psi}\end{bmatrix}+\boldsymbol{K}_D\begin{bmatrix}\dot e_\phi\\ \dot e_\theta\\ 0\end{bmatrix}+\boldsymbol{K}_I\begin{bmatrix}\int e_\phi dt\\ \int e_\theta dt\\ \int e_{\dot\psi} dt\end{bmatrix} \tag{26}$$

$$\boldsymbol{e}=\boldsymbol{y}_{\text{cmd}}-\boldsymbol{y}; \tag{27}$$

The 3-by-3 diagonal matrices $\boldsymbol{K}_P$, $\boldsymbol{K}_I$, and $\boldsymbol{K}_D$ identify the proportional, integral, and derivative gain matrices, respectively. The command model parameters adopted are shown in Table 5. Command model parameters are chosen to be the same as Ref. 30. Note that the coefficient matrices $(\boldsymbol{C}_1\boldsymbol{A}\boldsymbol{B})^{-1}, \boldsymbol{C}_1\boldsymbol{A}^2, (\boldsymbol{C}_2\boldsymbol{B})^{-1}$, and $\boldsymbol{C}_2\boldsymbol{A}$ are functions of the total speed of the aircraft V. For this reason, from a practical standpoint, these matrices are computed offline at incremental longitudinal speeds from hover to the maximum speed of the aircraft at 20 kt intervals and stored. When the linearized DI controller is implemented on the nonlinear aircraft dynamics, the coefficient matrices $(\boldsymbol{C}_1\hat{\boldsymbol{A}}\hat{\boldsymbol{B}})^{-1}$, $\boldsymbol{C}_1\boldsymbol{A}^2$, $(\boldsymbol{C}_2\boldsymbol{B})^{-1}$, and $\boldsymbol{C}_2\boldsymbol{A}$ are computed at each time step via interpolation based on the current airspeed $V(t)$ and on the lookup tables stored offline. It is important to note that what is implemented in the nonlinear aircraft dynamics is linearized DI. However, because the coefficient matrices are scheduled with the longitudinal speed, and scheduling effectively introduces a nonlinear relation between the aircraft states and the feedback control input, the controller implemented is effectively NDI (Ref. 29).

Outer-velocity loop

The objective of the outer-velocity loop is to track longitudinal and lateral velocities in the heading frame, such that the reference trajectory is given by

$$\boldsymbol{y}^T_{\text{cmd}}=\begin{bmatrix}V_{x_{\text{cmd}}} & V_{y_{\text{cmd}}} & V_{z_{\text{cmd}}}\end{bmatrix} \tag{28}$$

The heading frame is a vehicle-carried frame where the x-axis is aligned with the current aircraft heading, the z-axis is positive up in the inertial frame, and the y-axis points to the right, forming a left-handed orthogonal coordinate system. The following equation shows the rotation from the body to the heading frame:

$$\boldsymbol{T}_{B\to h}=\begin{bmatrix}\cos\theta & \sin\phi\sin\theta & \cos\phi\sin\theta\\ 0 & \cos\phi & -\sin\phi\\ \sin\theta & -\sin\phi\cos\theta & -\cos\phi\cos\theta\end{bmatrix} \tag{29}$$

such that the velocities in the heading frame are given by

$$\begin{bmatrix}V_x\\ V_y\\ V_z\end{bmatrix}=\boldsymbol{T}_{B\to h}\begin{bmatrix}u\\ v\\ w\end{bmatrix} \tag{30}$$

The outer-velocity loop is modified with respect to Ref. 15 not to include the auxiliary control input (i.e., the nacelle/wing angle in the case of the tilt-rotor) as a control variable. Rather, the nacelle/wing angle is prescribed based on flight speed but can still be adjusted via open-loop pilot inputs. While scheduling the nacelle/wing angle with flight speed is relatively straightforward, incorporating flap deflections and vertical speed could enhance robustness. This approach is used because the upper and lower limits of the conversion corridor are unknown for all aircraft considered in this study, except for the XV-15, and are challenging to derive due to complex power and structural limits, as well as whirl flutter. If the conversion corridor were known, the control law could be designed to follow its upper limit during acceleration and its lower limit during deceleration, as demonstrated in Ref. 15. The outer loop dynamics are designed based on the following reduced-order dynamics:

$$\begin{aligned}\begin{bmatrix}\dot u\\ \dot v\\ \dot w\end{bmatrix}&=\begin{bmatrix}X_u & 0 & 0\\ 0 & Y_v & 0\\ 0 & 0 & Z_w\end{bmatrix}\begin{bmatrix}u\\ v\\ w\end{bmatrix}+\begin{bmatrix}0 & X_\theta & X_{\delta_{\text{col}}}\\ Y_\phi & 0 & 0\\ 0 & Z_\theta & Z_{\delta_{\text{col}}}\end{bmatrix}\begin{bmatrix}\phi_{\text{cmd}}\\ \theta_{\text{cmd}}\\ \delta_{\text{col}}\end{bmatrix}\\ &=\boldsymbol{A}\boldsymbol{x}+\boldsymbol{B}\boldsymbol{u}\end{aligned} \tag{31a}$$

$$\begin{aligned}\begin{bmatrix}V_x\\ V_y\\ V_z\end{bmatrix}&=\begin{bmatrix}\cos\theta_0 & 0 & \sin\theta_0\\ 0 & 1 & 0\\ -\sin\theta_0 & 0 & \cos\theta_0\end{bmatrix}\begin{bmatrix}u\\ v\\ w\end{bmatrix}\\ &=\boldsymbol{C}\boldsymbol{x}\end{aligned} \tag{31b}$$

where $\boldsymbol{x}, \boldsymbol{u}$ are the reduced-order state, control input, and output vectors used for outer-loop control design; $\boldsymbol{A}, \boldsymbol{B}, \boldsymbol{C}$ are the system, control, and output matrices used for outer-loop control design; u, v, w are the longitudinal, lateral, and vertical velocities in the body-fixed frame; V_x, V_y, V_z are the longitudinal, lateral, and vertical velocities in the heading frame; $\phi_{\text{cmd}}, \theta_{\text{cmd}}$ are the roll and pitch attitudes commanded to the inner loop; $X_u, Y_v, Z_W, X_\theta, Y_{\delta_\phi}, Z_\theta$ are stability derivatives; $X_{\delta_{\text{col}}}, Z_{\delta_{\text{col}}}$ are stability derivatives, and θ_0 is the trim pitch attitude.

Then, the DI outer-loop control law will be of the form:

$$\boldsymbol{u}=(\boldsymbol{C}\boldsymbol{B})^{-1}(\boldsymbol{\nu}-\boldsymbol{C}\boldsymbol{A}\boldsymbol{x}) \tag{32}$$

where $\boldsymbol{\nu}$ is the pseudo-control vector. Like for the inner-velocity loop, the stability and control derivatives are a function of the total speed V, such that the coefficient matrices $(\boldsymbol{C}\boldsymbol{B})^{-1}$ and $\boldsymbol{C}\boldsymbol{A}$ are also functions of total speed. Thus, these matrices are computed at discrete speed increments and stored offline along with those of the inner loop. The reference trajectory is subtracted from the output to find the error, which is compensated by a PI controller. The feed-forward signal is subsequently added, leading to the pseudo-control vector for the outer loop:

$$\begin{bmatrix}\nu_{V_x}\\ \nu_{V_y}\\ \nu_{V_z}\end{bmatrix}=\begin{bmatrix}\dot V_{x_{\text{cmd}}}\\ \dot V_{y_{\text{cmd}}}\\ \dot V_{z_{\text{cmd}}}\end{bmatrix}+\boldsymbol{K}_P\begin{bmatrix}e_{V_x}\\ e_{V_y}\\ e_{V_z}\end{bmatrix}+\boldsymbol{K}_I\begin{bmatrix}\int e_{V_x} dt\\ \int e_{V_y} dt\\ \int e_{V_z} dt\end{bmatrix} \tag{33}$$

where $\boldsymbol{K}_P$ and $\boldsymbol{K}_I$ are 3-by-3 proportional and integral gain matrices, respectively. The command models for the longitudinal, lateral, and vertical speeds are first order, and their break frequencies are reported in Table 6.

Error dynamics

Feedback compensation gains that act on the error dynamics are designed according to the methods in Refs. 15, 29–31, 37, 39, 40, and 42. These methods are summarized as follows.

Table 7. Inner loop disturbance rejection frequencies, damping ratios, and integrator poles

	ω_n (rad/s)	ζ	p
ϕ_{cmd}	4.0	0.7	0.75
θ_{cmd}	3.5	0.7	0.75
$\dot{\psi}_{\text{cmd}}$	2	1	–

Table 8. Outer loop disturbance rejection frequencies and damping ratios

	ω_n (rad/s)	ζ
$V_{x_{\text{cmd}}}$	0.5	1
$V_{y_{\text{cmd}}}$	0.5	1
$V_{z_{\text{cmd}}}$	0.5	1

Feedback compensation is needed to ensure the system tracks the command models. It can be demonstrated (Ref. 49) that for a DI control law the output equation must be differentiated n times for the controls to appear explicitly in the output equation:

$$e^{(n)} = y_{\text{cmd}}^{(n)} - \nu \tag{34}$$

For the output equations that require to be differentiated only once, a PI control strategy is applied to the pseudo-command vector:

$$\nu = \dot{y}_{\text{cmd}}(t) + K_P e(t) + K_I \int_0^t e(\tau)d\tau \tag{35}$$

Substituting Eq. (35) into Eq. (34) leads to the closed-loop error dynamics:

$$\dot{e}(t) + K_P e(t) + K_I \int_0^t e(\tau)d\tau = 0 \tag{36}$$

The gains are chosen such that the frequencies of the error dynamics are of the same order as the command filters (i.e., first order), ensuring that the bandwidth of the response to disturbances is comparable to that of an input given by a pilot or outer loop. By taking the Laplace transform, and therefore switching to the frequency domain, the error dynamics become

$$e(s)(s^2 + sK_P + K_I) = 0 \tag{37}$$

To obtain the gains that guarantee the desired response, the error dynamics of Eq. (37) are set equal to the following second-order system:

$$s^2 + 2\zeta\omega_n s + \omega_n^2 = 0 \tag{38}$$

yielding the following proportional and integral gains:

$$K_P = 2\zeta\omega_n \tag{39a}$$

$$K_I = \omega_n^2 \tag{39b}$$

Similarly, for those outputs that require to be differentiated twice, a PID control strategy is applied to the pseudo-command vector:

$$\nu = \ddot{y}_{\text{cmd}}(t) + K_D\dot{e}(t) + K_P e(t) + K_I \int_0^t e(\tau)d\tau \tag{40}$$

Substituting Eq. (40) into Eq. (34) leads to the following closed-loop error dynamics:

$$\ddot{e}(t) + K_D\dot{e}(t) + K_P e(t) + K_I \int_0^t e(\tau)d\tau = 0 \tag{41}$$

and, therefore, to

$$e(s)(s^3 + K_D s^2 + K_P s + K_I) = 0 \tag{42}$$

Again, the gains are chosen such that the frequencies of the error dynamics are of the same order as the command filters (i.e., second order), ensuring that the bandwidth of the response to disturbances is comparable to that of an input given by a pilot or outer loop. To obtain the gains that guarantee the desired response, the error dynamics of Eq. (42) are set equal to the following third-order system:

$$\left(s^2 + 2\zeta\omega_n s + \omega_n^2\right)(s + p) = 0 \tag{43}$$

yielding the following proportional, integral, and derivative gains

$$K_D = 2\zeta\omega_n + p \tag{44a}$$

$$K_P = 2\zeta\omega_n p + \omega_n^2 \tag{44b}$$

$$K_I = \omega_n^2 p \tag{44c}$$

This compensation strategy is used for ensuring trajectory tracking in both the inner and outer loops. Tables 7 and 8 show the natural frequencies, damping ratios, and the integrator pole values used to compute the inner and outer loop gains. These values are common across rotorcraft. Note that the integrator pole p is usually chosen to be one-fifth of the natural frequency, corresponding to about one-fifth of the loop crossover frequency (Ref. 50). Further, the outer loop error dynamics natural frequency must be 1/10 to 1/5 of the inner loop error dynamics natural frequency to ensure sufficient frequency separation (Ref. 50). Additionally, because the plant is inverted in the feedback linearization loop such that the system being controlled is effectively a set of integrators, there is no need for gain scheduling. However, the plant model used for feedback linearization must still be scheduled with the flight condition (i.e., with the aircraft speed V in this case).

Turn coordination

Because the tilt-rotor/wing flight envelope includes low-speed flight (i.e., lower than approximately 50 kt) as well as high-speed flight (i.e., greater than 50 kt), different control strategies are necessary to control the yaw rate for these two flight conditions. Above 50 kt, turn coordination is used; below 50 kt, no turn coordination (Ref. 51) is used. These control strategies are summarized as follows:

$$\phi'_{\text{cmd}} = \begin{cases} \phi_{\text{cmd}}, & V < V_{\text{HS}} \\ \tan^{-1}\left(\frac{V}{g}\dot{\psi}_{\text{cmd}}\right), & V \geq V_{\text{HS}} \end{cases} \tag{45}$$

where $V_{\text{HS}} = 50$ kt.

Results

Validation

The XV-15-like simulation model is validated both in the frequency and time domains against US Army/NASA flight-test (Ref. 52) data and other models in the literature (Ref. 53). The rotorcraft is trimmed at hover in helicopter mode (i.e., with the nacelles at $\beta_{\text{R}} = 0$ deg according to the definition in Ref. 32) and at 170 kt in aircraft mode (i.e., with the nacelles at $\beta_{\text{R}} = 90$ deg) for validation. Figure 5 shows a comparison of the lateral dynamics eigenvalues for each of these conditions with those from US Army/NASA flight-test data (Ref. 52) and from Ref. 53. Notably, the linearized dynamics eigenvalues are close to those of both the system identified dynamics from Ref. 52, and those of the FLIGHTLAB® simulation model from Ref. 53. Moreover, the residualized dynamics eivencalues nearly overlap those of the full-order dynamics, indicating the accuracy of the model-order reduction method used. Figure 6 shows

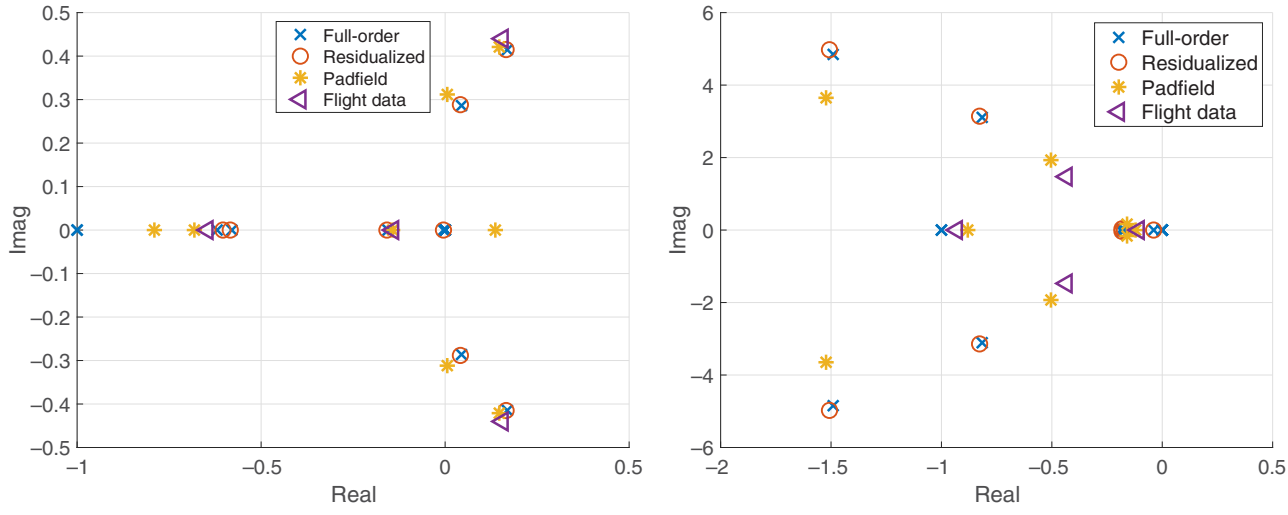

(a) Hover (b) 170 kt

Fig. 5. Comparison of the XV-15 lateral dynamics eigenvalues with those from US Army/NASA flight-test data (Ref. 52) and simulation data from Ref. 53.

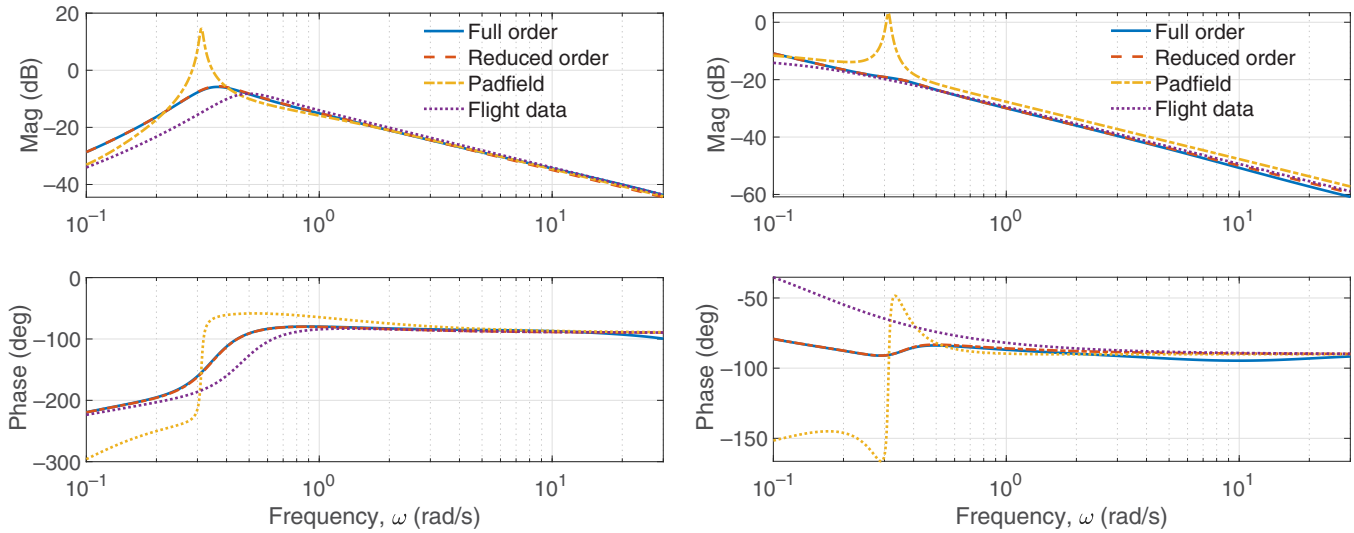

(a) p/δ_{lat} (b) r/δ_{ped}

Fig. 6. Bare-airframe frequency responses at hover compared with US Army/NASA XV-15 flight data (Ref. 52) and simulation data from Ref. 53.

some sample frequency responses at hover as compared to US Army/NASA XV-15 flight data (Ref. 52) and simulation data from Ref. 53. Again, the linearized dynamics are very close to those from flight-test data and the model in the literature, and the residualized model overlaps the full-order frequency response. While for the cases presented the general agreement is good, the available flight-test data do not provide the exact information on Center of Gravity (CG) location, moments of inertia, weight, and flap setting. As such, it is difficult to draw definitive conclusions.

To provide additional validation, time-domain responses are computed for the nonlinear, linearized full order, and residualized dynamics at hover based on lateral dynamics pilot control inputs from US Army/NASA flight-test data (Ref. 52), shown in Fig. 7(a). The lateral dynamics response is shown in Fig. 7(b), where it is compared with flight-test data and the simulated response of the dynamics from Ref. 53. This figure shows a generally good agreement between the nonlinear simulation model and the flight-test data and also between the nonlinear simulation model and the data from Padfield (Ref. 53). It is also important to note that both full-order and residualized dynamics nearly overlap the nonlinear simulation, which indicates the accuracy of the linearized models and validates the model-order reduction strategy. In this sense, residualized models are accurate enough to be used for control design.

Trim

As a first step, the simulation models are trimmed at incremental flight speed from 0 to 280 kt for the TR configuration and from 0 to 200 kt for the TMR, TMR2, and TW configurations. Note that, for the TR configuration, the auxiliary control input (i.e., nacelle tilt angle) is prescribed since the XV-15 conversion corridor is known (Ref. 54). The prescribed tilt angle approximately corresponds to the center of the conversion corridor. On the other hand, because for the TMR and TW configurations

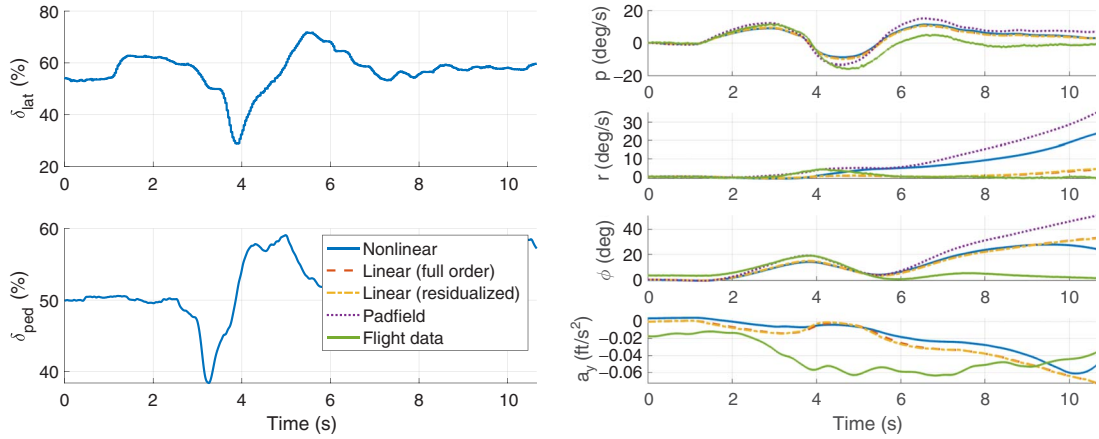

(a) Pilot inputs (b) Lateral dynamics states

Fig. 7. GenTR time response to pilot inputs at hover as compared with US Army/NASA XV-15 flight-test data.

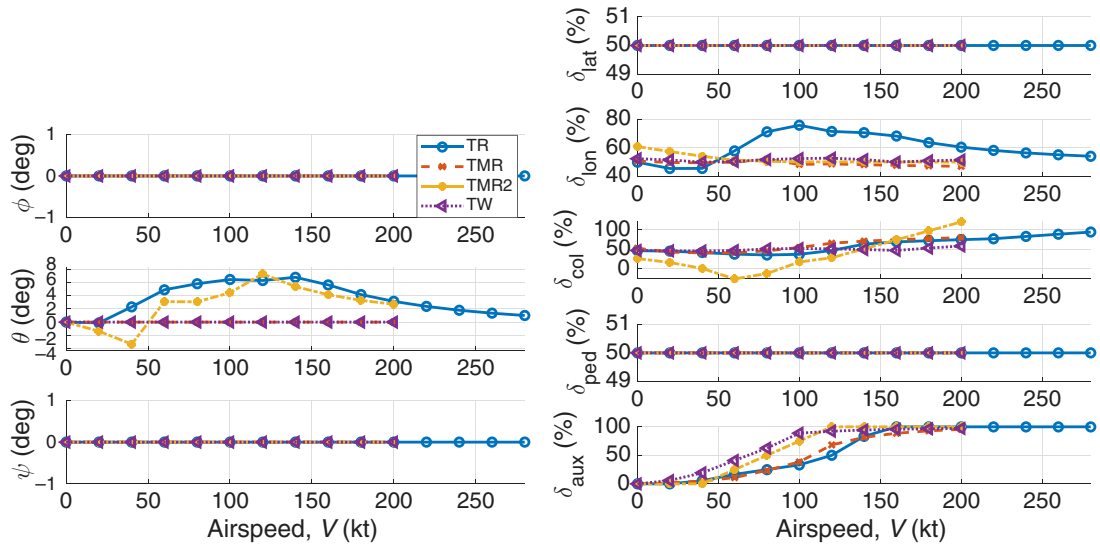

(a) Euler angles (b) Control inputs

Fig. 8. Trim variables for increasing speed.

the conversion corridor is unknown, the auxiliary control input is used as a control variable in place of the pitch attitude. More specifically, the pitch attitude is prescribed to zero while the auxiliary control input is an unknown variable in the trim process. The TMR2 conversion corridor is also unknown, but it was not possible to trim the flight dynamics at zero pitch attitude at every flight speed and, as such, a prescribed rotor tilt angle profile with speed was assumed. The trim attitude and pilot control inputs are shown in Fig. 8 for all aircraft. More specifically, Fig. 8(a) shows the trim Euler angles for increasing flight speed. While trim roll and yaw attitudes are zero across the flight speed considered, which stems from the tilt-rotor/wing vehicles in consideration of being symmetric about the $x-z$ plane, the trim pitch attitude behaves differently. In fact, for both TR and TMR2 configurations, the trim pitch attitude is shown to increase with increasing speed up to 120 kt, and subsequently steadily decrease as it would for a fixed-wing aircraft (Ref. 55). Since the TMR and TW configurations are trimmed with zero pitch attitude, and given the symmetry of the configurations about the $x-z$ plane, the trim roll, pitch, and yaw attitudes are all zero for this configurations.

Figure 8(b) shows the trim pilot stick inputs for increasing speed. In this figure, the lateral stick and pedals are shown to remain at the neutral position due to the symmetry of the aircraft about the $x-z$ plane. The longitudinal stick loosely follows the trend of the pitch attitude for the TR configuration, while it remains approximately neutral for the TMR and TW models. Trim collective stick inputs first decrease due to the lower power required in low-speed forward flight compared to hover, and subsequently steadily increase with flight speed. Nacelle control inputs for the TR and TMR2 turn out to be similar, as the nacelles are shown to tilt from 0 to -90 deg between 40 and 160 kt. On the other hand, the TMR2 and TW conversion starts and ends at lower speeds, with a final transition happening at approximately 100.

Figure 9 shows the trim actuator inputs for each aircraft. The rotor speed of the TR, TMR, and TW configurations is scheduled with speed (Figs. 9(a), 9(b), and 9(d)) and drops to 85% of its hover value at high speeds. On the other hand, the TMR2 configuration, which is RPM-controlled, features scheduled collective pitch inputs with speed. More particularly, collective pitch is scheduled to increase from hover

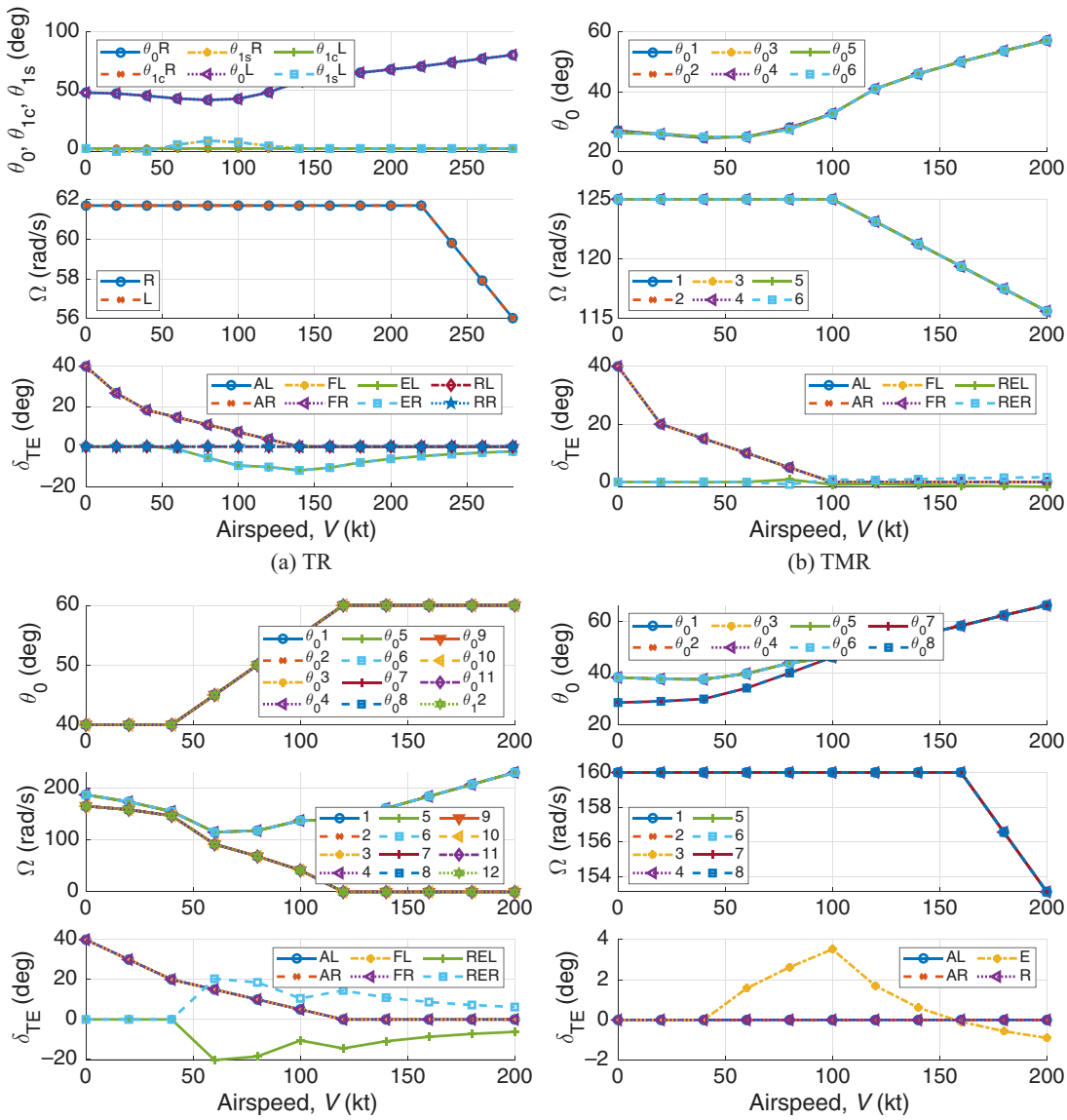

Fig. 9. Actuator inputs for increasing speed.

to cruise flight (Fig. 9(c)). All configurations but the TW adopt flaps, which are also scheduled with speed. A common value of 40 deg is used for hover and low-speed flight, which drops to 20 deg during the initial stages of the transition, to then settle to 0 deg at higher speeds. The use of flaps in these configurations is based on an informed estimation, as no publicly available data exists on flap usage for any configuration except the TR configuration. Therefore, the integration of flaps in this study should be regarded as a representative example rather than a precise replication of actual flap deployment strategies. The assumed scheduling of flaps with speed is intended to demonstrate the methodology's applicability across different configurations rather than to accurately capture specific aircraft designs. Figure 9 also shows the trim positions of various trailing-edge control surfaces, which may (i) include right or left ailerons ("AR," "AL"); (ii) right or left flaps ("FR," "FL"); (iii) right, left, or sole elevators ("RE," "LE," "E"); (iv) right, left, or sole rudders ("RR," "LR," "R"); and (v) and right or left ruddervators for the V-tail configurations ("RER," "REL"). Finally, this figure features the rotor swashplate inputs. Note that while the TR configuration uses collective (θ_0), lateral cyclic (θ_{1c}), and longitudinal cyclic (θ_{1s}), all other configurations only adopt collective pitch control.

Handling qualities

Closed-loop performance is assessed in the frequency domain by evaluating selected stability, performance, and handling-quality metrics. For brevity, only hover results are presented in this analysis. This evaluation considers the following components: (i) a flight control computer operating at 100 Hz, resulting in a processing delay and a digital-to-analog sample-and-hold delay of $\tau = 50$ ms each; (ii) actuators modeled with second-order dynamics and bandwidths of 8 Hz (approximately 50.27 rad/s); (iii) sensors represented as second-order filters with bandwidths of 5 Hz (equivalently, 31.42 rad/s); and (iv) an additional sensor transport delay of $\tau = 20$ ms to account for sampling skew and bus transport delays (Ref. 50).

The first metrics evaluated are the gain and phase margins (GM/PM), commonly referred to as stability margins, which pertain to the on-axis

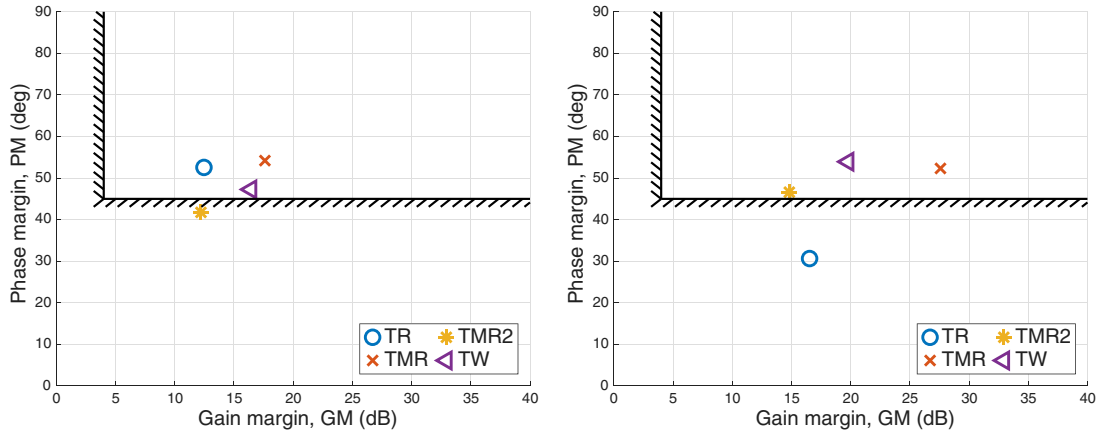

(a) BL_{ϕ} (b) BL_{θ}

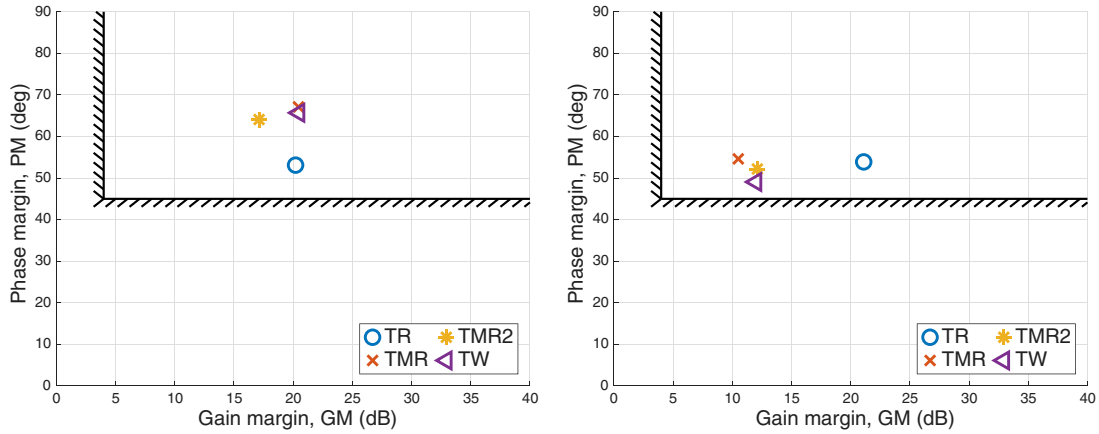

(c) BL_{ψ} (d) BL_{V_x}

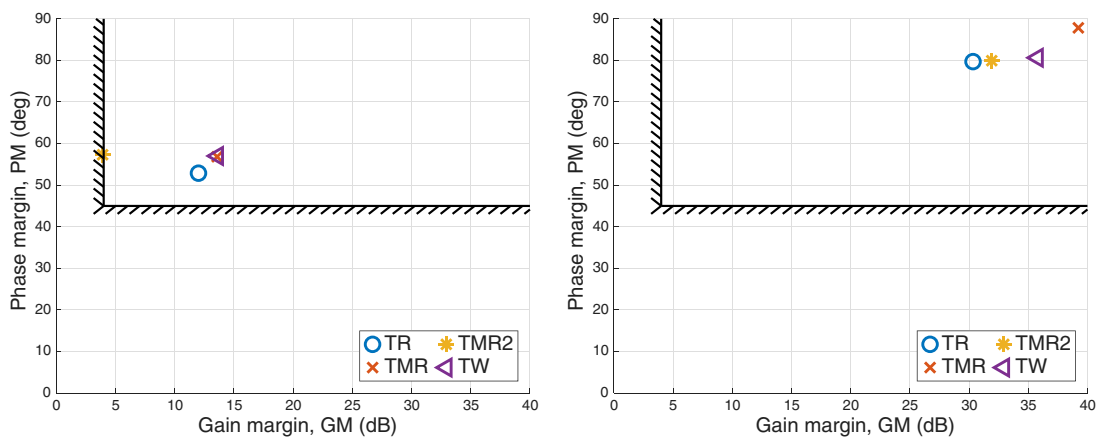

(e) BL_{V_y} (f) BL_{V_z}

Fig. 10. Hover stability margins.

broken-loop response. While general stability margin guidelines are provided in SAE AS94900 (Ref. 56), which recommends a phase margin of 45 deg and a gain margin of at least 6 dB for robust feedback control, past work has shown that reducing the gain margin requirement to 4 dB—while retaining the standard phase margin—can improve performance without compromising handling qualities (Refs. 57, 58). Accordingly, this work adopts the reduced gain margin of 4 dB from Refs. 57 and 58 and the phase margin of 45 deg from Ref. 56 in assessing broken-loop response for level 1 handling qualities. The gain and phase margins for each controlled axis in the inner-attitude and outer-velocity loops, for all aircraft, are presented in Fig. 10. As shown in this figure, the gain and phase margins generally meet the specified criteria for all aircraft.

The second metric assessed comprises the disturbance rejection bandwidth and peak (DRB/DRP) (Ref. 59). The requirements for these metrics vary across different axes. The results are presented in Fig. 11 for each controlled axis and aircraft. Similar to the gain and phase margins,

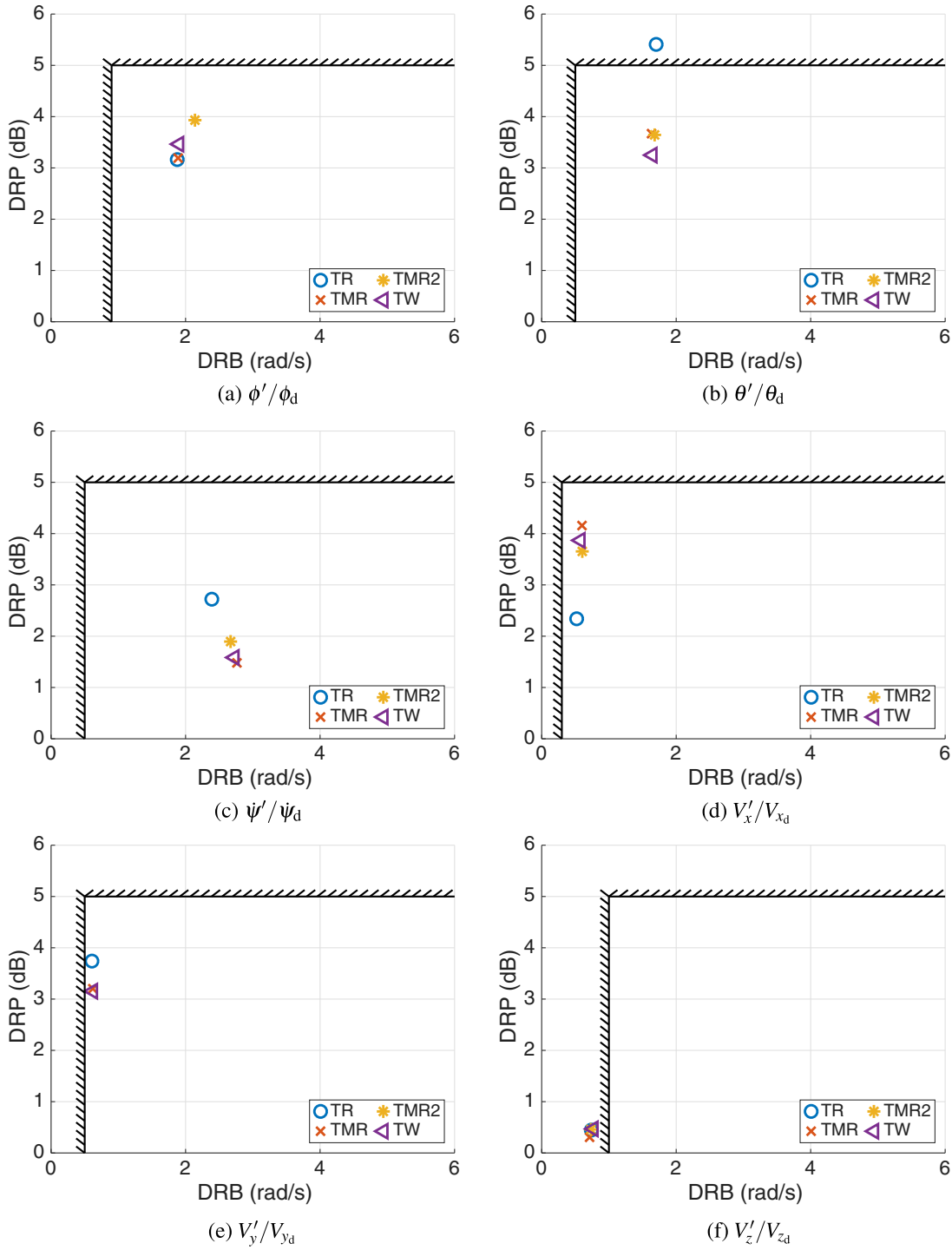

(a) ϕ'/ϕ_{d} (b) $\theta'/\theta_{\mathrm{d}}$

(c) ψ'/ψ_{d} (d) $V_x'/V_{x_{\mathrm{d}}}$

(e) $V_y'/V_{y_{\mathrm{d}}}$ (f) $V_z'/V_{z_{\mathrm{d}}}$

Fig. 11. Hover disturbance rejection bandwidth and peak (DRP/DRB).

these criteria are generally satisfied, with only a few instances where the metrics are close to or slightly outside the specified boundaries, suggesting overall effective disturbance rejection performance.

The third and final set of results involves comparing the closed-loop response with the command models employed for each axis in the frequency domain. These results are illustrated in Fig. 12 and generally demonstrate good on-axis tracking across all axes and aircraft, with the exception of suboptimal longitudinal speed command tracking for the TR configuration above approximately 1 rad/s, as highlighted in Fig. 12(d). Overall, these results suggest that the control system design achieves satisfactory performance in terms of stability, disturbance rejection, and reference tracking within the specified operational envelope.

Automatic transition

The rotorcraft flight dynamics are linearized and residualized at each discrete speed increment to obtain the DI control law coefficient matrices. DI control laws are demonstrated for closed-loop simulations of an acceleration from hover to cruise flight, which includes a conversion from helicopter to airplane mode. The simulation consists of

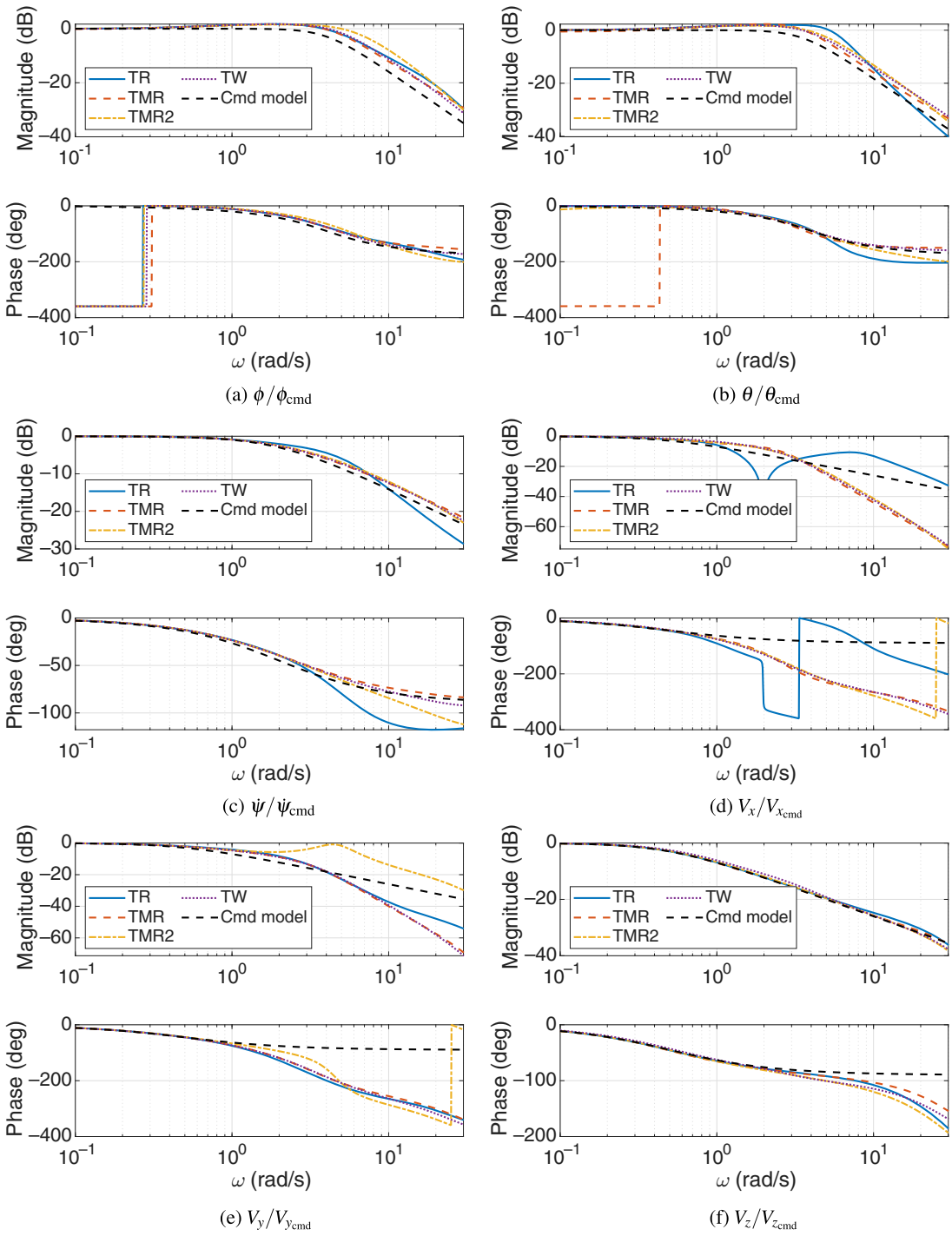

Fig. 12. Hover on-axis closed-loop responses compared to the command models.

an acceleration from hover to 160 kt over 60 seconds. This simulation makes use of the nonlinear rotorcraft dynamics. Figure 13(a) shows the heading-frame velocities. In this figure, the longitudinal speed is shown to track accurately the reference trajectory while the off-axis responses in lateral and vertical speed are minimal. Figure 13(b) shows how the inner-attitude loop is able to track the desired pitch attitude while maintaining zero roll and yaw attitudes. The pitch attitude first decreases to direct the rotor thrust forward and thus accelerates, and then gradually increases as the aircraft reaches a steady acceleration. Finally, Fig. 14 shows the bare-airframe inputs for each rotorcraft. Actuator inputs are shown to follow a similar time evolution to that shown in Fig. 9.

A second 60-s transition simulation consisting of acceleration from hover to cruise flight at 160 kt, while undergoing a 90-deg turn during a 600 ft/min climb, is shown in Fig. 15 to demonstrate the performance of the flight control laws in the lateral axis. The rotorcraft begins from a hover condition and starts accelerating at the sixth second of simulation, as shown in Fig. 15(a). At the 18th second, the rotorcraft starts climbing at 600 ft/min (also shown in Fig. 15(b)), and at approximately 26.2 s, the rotorcraft enters a right turn at $\dot{\psi} = 0.1$ rad/s. Because the rotorcraft is

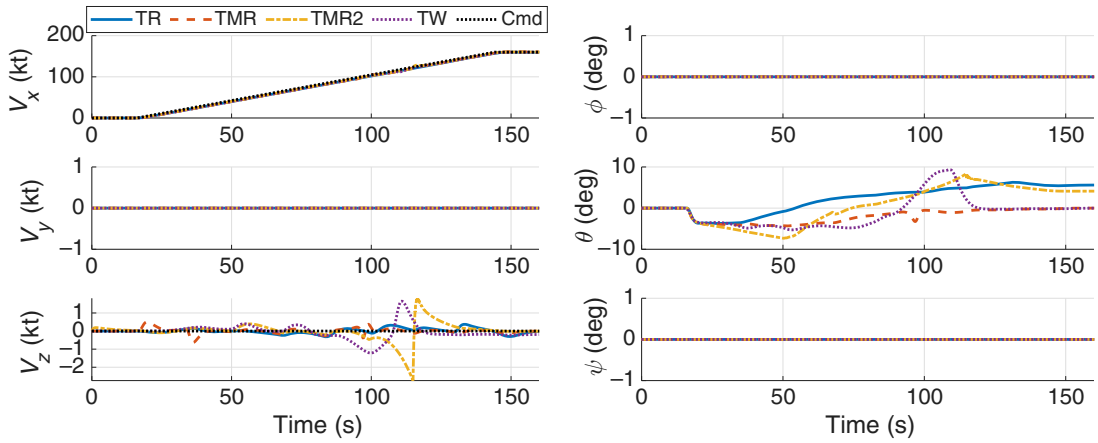

(a) Heading-frame velocities (b) Euler angles

Fig. 13. Transition from hover (helicopter mode) to high-speed forward flight (airplane mode).

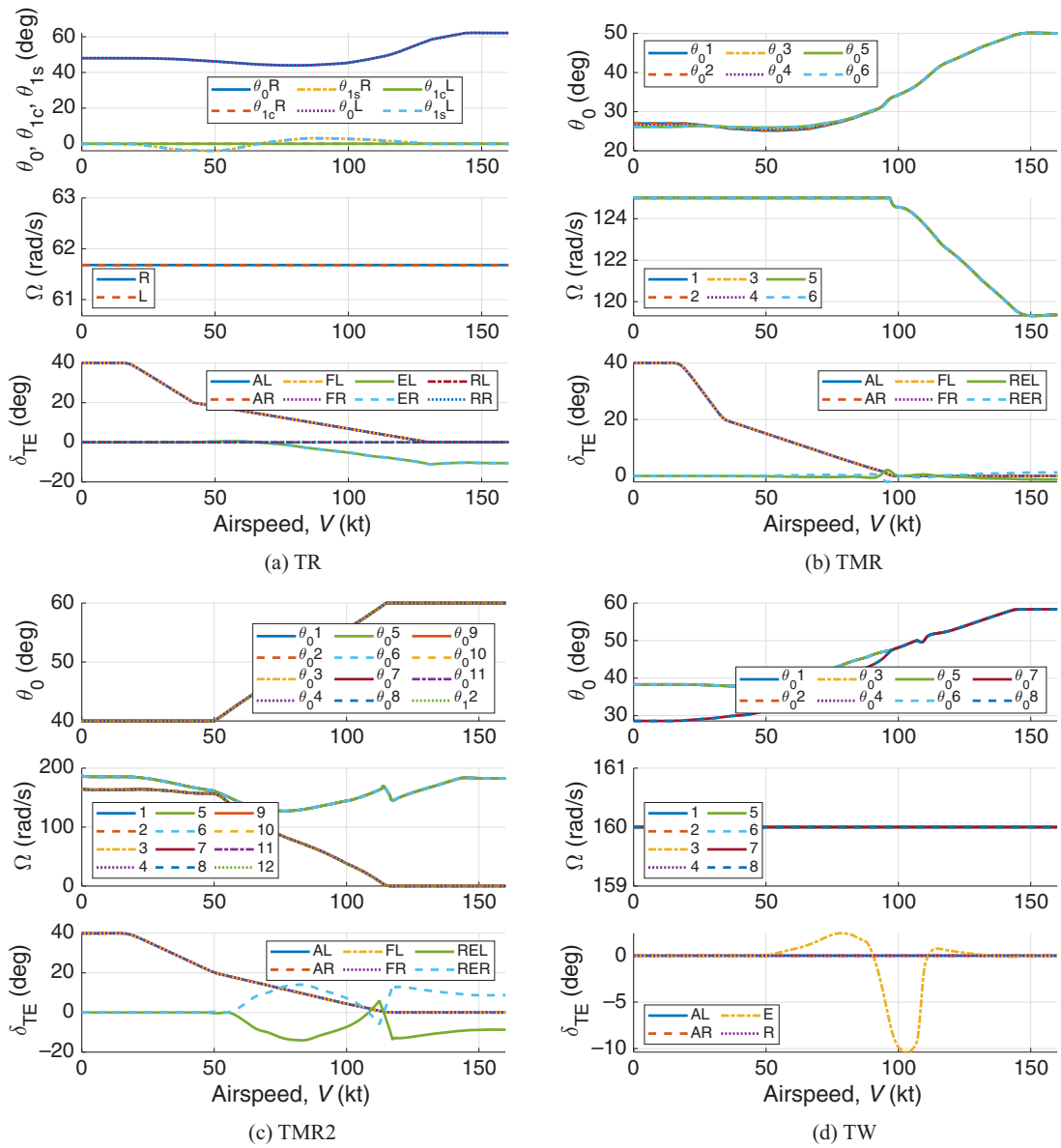

(a) TR (b) TMR

(c) TMR2 (d) TW

Fig. 14. Actuator inputs for a transition from hover (helicopter mode) to high-speed forward flight (airplane mode).

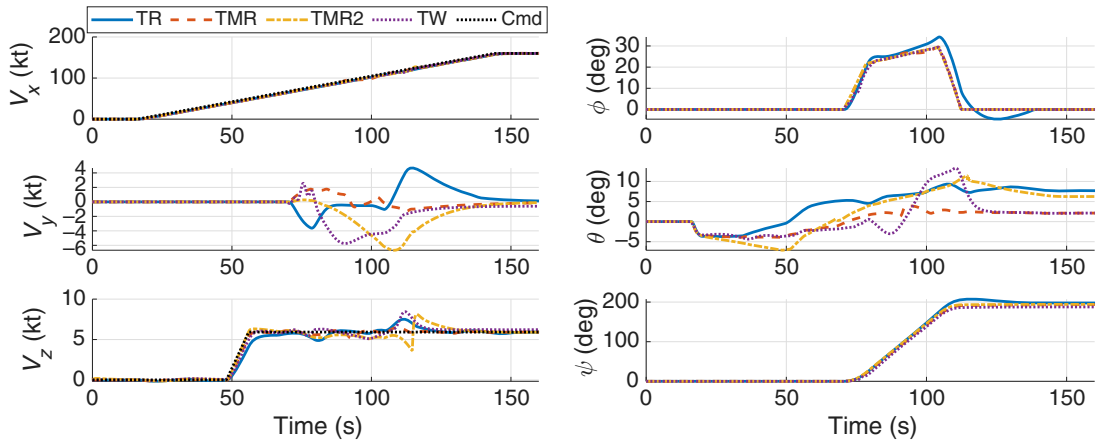

(a) Heading-frame velocities (b) Euler angles

Fig. 15. Transition from hover to high-speed forward flight with a 90-deg turn during a 600 ft/min climb.

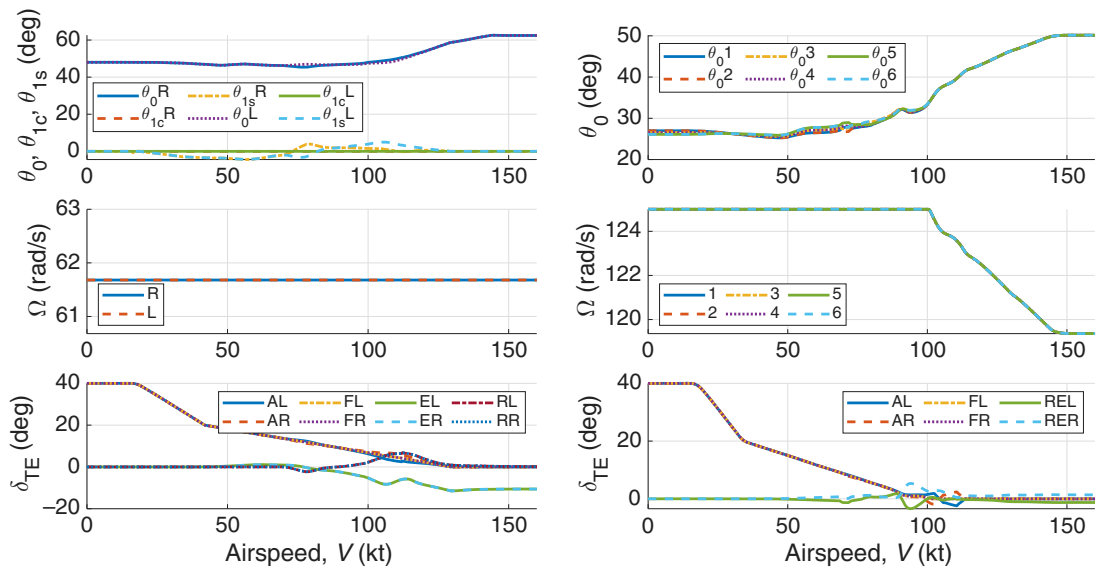

(a) TR (b) TMR

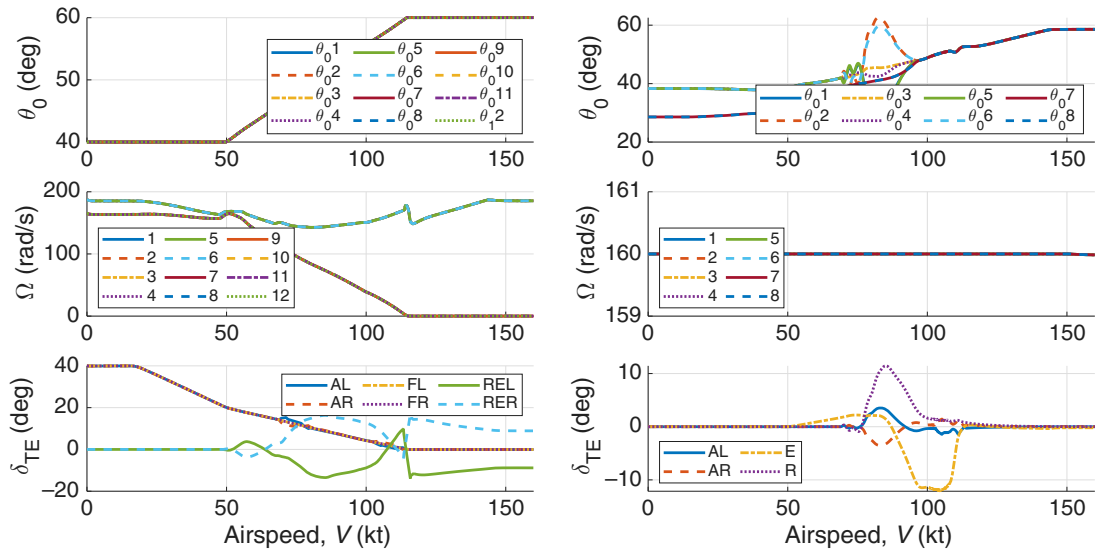

(c) TMR2 (d) TW

Fig. 16. Actuator inputs for a transition from hover to high-speed forward flight with a 90-deg turn during a 600 ft/min climb.

accelerating, and because the bank angle required for turn coordination is given by $\phi = \text{atan}(\frac{\dot{\psi}V}{g})$, as the airspeed V increases, the bank angle ϕ also increases during the turn. The resulting steady increase in heading angle is shown in Fig. 15(b). The turn is maintained up to 42 s, whereas the acceleration stops at 54 s. The climb rate, on the other hand, is held until the end of the simulation. As with the previous simulation, the outer-velocity loops track the commanded velocities. However, some deviation from the commanded vertical speed is observed for all rotorcraft as the rotors tilt forward. Additionally, the inner-attitude loop is shown to track the roll, pitch, and yaw attitudes commanded by the outer-velocity loop. Like for the previous case, the actuator inputs shown in Fig. 16 follow a similar time evolution to that shown in Figs. 9 and Fig. 14, albeit with some added dynamics corresponding to the actuator input use during the turn.

Conclusions

A generic multirotor/wing simulation model was adapted to represent the flight dynamics of four tilt-rotor/wing configurations: a tilt-rotor aircraft similar to a Bell XV-15, two tilt-rotor eVTOL aircraft reminiscent of Joby S4 and Archer Midnight vehicles, respectively, and a tilt-wing aircraft similar to the NASA Tilt Wing. To verify the correct implementation of the generic multirotor/wing flight dynamics code, the XV-15-like simulation model was validated in both the frequency and time domains against US Army/NASA flight-test data and other models in the literature. The rotorcraft flight dynamics were trimmed at discrete speed increments from hover to cruise flight and then linearized. Model-order reduction methods were employed to reduce the order of these linearized models, making them suitable for flight control design.

NDI control laws were developed and implemented to enable automatic transition given a prescribed profile of rotor tilt angle with aircraft speed. These control laws were demonstrated in batch simulations for all aircraft configurations, resulting in successful automatic transitions from hover (helicopter mode) to cruise (airplane mode) flight, with excellent tracking of the commanded forward speed and minimal off-axis response.

While the results demonstrate the potential of the proposed NDI control architecture for enabling transitioning flight in tilt-rotor/wing aircraft, this work remains exploratory. The conclusions are limited by the high-level nature of the control architecture and do not account for detailed design considerations, such as control authority, actuator constraints, or structural loads. A more comprehensive evaluation, including piloted handling qualities assessments and robustness analyses, will be necessary to validate the suitability and practicality of the proposed control laws for operational use.

Acknowledgments

This research was partially funded by the U.S. Government under agreement no. 314380-00001 with System Technology, Inc. (STI) as prime sponsor. The views and conclusions contained in this document are those of the authors and should not be interpreted as representing the official policies, either expressed or implied, of the Aviation Development Directorate or the U.S. Government.

References

[1]Lopez, M. J. S., Padthe, A. K., Glover, E. D., Berger, T., and Tobias, E. L., "Seeking Lift Share: Design Trade-offs for a Winged Single Main Rotor Helicopter," Proceedings of the 78th Annual Forum of the Vertical Flight Society, Fort Worth, TX, May 10–12, 2022. doi: https://doi.org/10.4050/F-0078-2022-17547.

[2]Padthe, A. K., Lopez, M. J. S., Berger, T., Juhasz, O., Tobias, E. L., and Glover, E. D., "Design, Modeling, and Flight Dynamics Analysis of Generic Lift-Offset Coaxial Rotor Configurations," Proceedings of the 78th Annual Forum of the Vertical Flight Society, Fort Worth, TX, May 10-12, 2022. doi: https://doi.org/10.4050/F-0078-2022-17580.

[3]Berger, T., Juhasz, O., Lopez, M. J. S., Tischler, M. B., and Horn, J. F., "Modeling and Control of Lift Offset Coaxial and Tiltrotor Rotorcraft," Proceedings of the 78th Annual Forum of the Vertical Flight Society, September 19–20, 2018.

[4]Berger, T., Juhasz, O., Lopez, M. J. S., Tischler, M. B., and Horn, J. F., "Modeling and Control of Lift Offset Coaxial and Tiltrotor Rotorcraft," *CEAS Aeronautical Journal*, Vol. 11, 2024, pp. 191–215. doi: https://doi.org/10.1007/s13272-019-00414-0.

[5]Straubinger, A., Rothfeld, R., Shamiyeh, M., Bütcher, K. D., Kaiser, J., and Plötner, K. O., "An Overview of Current Research and Developments in Urban Air Mobility – Setting the Scene for UAM Introduction," *Journal of Air Transport Management*, **87**, 101852 (2020). doi: https://doi.org/10.1016/j.jairtraman.2020.101852.

[6]Sliva, C., Johnson, W., Antcliff, K. R., and Patterson, M. D., "VTOL Urban Air Mobility Concept Vehicles for Technology Development," AIAA 2018-3847, Proceedings of the 2018 Aviation Technology, Integration, and Operations Conference, Atlanta, GA, June 25–29, 2018. doi: https://doi.org/10.2514/6.2018-3847.

[7]Sobiesiak, L. A., Fortier-Topping, H., Beaudette, D., and Bolduc-Teasdale, F., "Modelling and Control of Transition Flight of an eVTOL Tandem Tilt-Wing Aircraft," Proceedings of the 8th European Conference for Aeronautics and Aerospace Sciences (EUCASS), Madrid, Spain, July 1–4, 2019. doi: https://doi.org/10.13009/EUCASS2019-137.

[8]May, M., Milz, D., and Looye, G., "Transition Strategies for Tilt-Wing Aircraft," Proceedings of the AIAA SCITECH 2024 Forum, Orlando, FL, January 8–12, 2024. doi: https://doi.org/10.2514/6.2024-1289.

[9]Totoki, H., Ochi, Y., Sato, M., and Muraoka, K., "Design and Testing of a Low-Order Flight Control System for Quad-Tilt-Wing UAV," *Journal of Guidance, Control, and Dynamics*, Vol. 39, (10), 2016, pp. 2423–2430. doi: https://doi.org/10.2514/1.G001577.

[10]Comer, A. M., and Chakraborty, I., "Full Envelope Flight Control System Design and Optimization for a Tilt-Wing Aircraft," *Journal of the American Helicopter Society*, **69**, 032003 (2024). doi: https://doi.org/10.4050/JAHS.69.032003.

[11]Fu, R., Sun, H., and Zeng, J., "Exponential Stabilisation of Nonlinear Parameter-Varying Systems with Applications to Conversion Flight Control of a Tilt Rotor Aircraft," *International Journal of Control*, Vol. 92, (11), 2018, pp. 2473–2483. doi: https://doi.org/10.1080/00207179.2018.1442022.

[12]Yan, X., Chen, R., Lou, B., Xie, Y., Xie, A., and Zhang, D., "Study on Control Strategy for Tilt-Rotor Aircraft Conversion Procedure," *Journal of Physics*, Vol. 1924, 012010 (2021). doi: https://doi.org/10.1088/1742-6596/1924/1/012010.

[13]Flores, G., and Lozano, R., "Transition Flight Control of the Quad-Tilting Rotor Convertible MAV," Proceedings of the International Conference on Unmanned Aircraft Systems (ICUAS), Atlanta, GA, May 28–31, 2013. doi: https://doi.org/10.1109/ICUAS.2013.6564761.

[14]Rysdyk, R. T. and Calise, A. J., "Adaptive Model Inversion Flight Control for Tilt-Rotor Aircraft," *Journal of Guidance, Control, and Dynamics*, Vol. 22, (3), 1999, pp. 402–407. doi: https://doi.org/10.2514/2.4411.

[15]Berger, T., Tischler, M. B., and Horn, J. F., "Outer-Loop Control Design and Simulation Handling Qualities Assessment for a Coaxial-Compound Helicopter and Tiltrotor," Proceedings of the 77th Annual

Forum of the Vertical Flight Society, Virtual, October 5–8, 2020. doi: https://doi.org/10.4050/F-0076-2020-16392.

[16]Milz, D., and Looye, D., "Tilt-Wing Control Design for a Unified Control Concept," Proceedings of the AIAA SCITECH 2022 Forum, San Diego, CA, January 3–7, 2022. doi: https://doi.org/10.2514/6.2022-1084.

[17]Hartmann, P., Meyer, C., and Moormann, D., "Unified Velocity Control and Flight State Transition of Unmanned Tilt-Wing Aircraft," *Journal of Guidance, Control, and Dynamics*, Vol. 40, (6), 2017, pp. 1348–1359. doi: https://doi.org/10.2514/1.G002168.

[18]Qu, S., Zhu, G., Su, W., and Swei, S. S. M., "Linear Parameter-Varying-Based Transition Flight Control Design for a Tilt-Rotor Aircraft," *Journal of Aerospace Engineering*, Vol. 236, (16), 2022, pp. 2423–2430. doi: https://doi.org/10.1177/09544100221083713.

[19]Yomchinda, T., and Horn, J. F., "Integrated Flight Control Design and Handling Qualities Analysis for a Tilt Rotor Aircraft," Proceedings of the AIAA Atmospheric Flight Mechanics Conference, Chicago, IL, August 10–13, 2009. doi: https://doi.org/10.2514/6.2009-6058.

[20]Anon, "Handling Qualities for Military Rotorcraft," Technical Report, Department of Defense, MIL-DTL-32742, Redstone Arsenal, AL, 2023.

[21]Tobias, E. L., and Tischler, M. B., "A Model Stitching Architecture for Continuous Full Flight-Envelope Simulation of Fixed-Wing Aircraft and Rotorcraft from Discrete-Point Linear Models," Technical Report, U.S. Army AMRDEC Special Report RDMR-AF-16-01, Ames, CA, April 2016.

[22]Leishman, J. G., *Principles of Helicopter Aerodynamics*, Cambridge University Press, New York, NY, 2006.

[23]Pitt, D. M., and Peters, D. A., "Theoretical Prediction of Dynamic-Inflow Derivatives," Proceedings of the 6th European Rotorcraft and Powered Lift Aircraft Forum, Bristol, UK, September 16–19, 1980.

[24]Guner, F., and Prasad, J. V. R., "Combined Momentum Theory and Simple Vortex Theory Inflow Model for Multirotor Configurations," *Journal of the American Helicopter Society*, **67**, 022007 (2022). doi: https://doi.org/10.4050/JAHS.67.022007.

[25]Guner, F., "A Multirotor Inflow Model Based on Combined Momentum Theory and Simple Vortex Theory (CMTSVT) for Flight Simulations," Proceedings of the 78th Annual Forum of the Vertical Flight Society, Fort Worth, TX, May 10–12, 2022. doi: https://doi.org/10.4050/F-0078-2022-17579.

[26]Saetti, U., and Guner, F., "Interactional Aerodynamics Modeling and Flight Control Design of Multi-Rotor Aircraft," Proceedings of the 6th Decennial Aeromechanics Specialists' Conference, Santa Clara, CA, February 6–8, 2024.

[27]Jun, D., Cocco, A., Saetti, U., and Juhasz, O., "Flight Dynamics of a Coaxial Compound Helicopter with Rotor-On-Rotor Interactional Aerodynamics," Proceedings of the 50th European Rotorcraft Forum, Venice, Italy, September 10–12, 2024.

[28]Heyson, H. H., "Equations for the Induced Velocities Near a Lifting Rotor with Nonuniform Azimuthwise Vorticity Distribution," Technical Report, NASA TN D-394, 1960.

[29]Horn, J. F., "Non-Linear Dynamic Inversion Control Design for Rotorcraft," *Aerospace*, **6**, 38 (2019). doi: https://doi.org/10.3390/aerospace6030038.

[30]Saetti, U., and Horn, J. F., "Tiltrotor Simulations with Coupled Flight Dynamics, State-Space Aeromechanics, and Aeroacoustics," *Journal of the American Helicopter Society*, **69**, 012003 (2024). doi: https://doi.org/10.4050/JAHS.69.012003.

[31]Saetti, U., Horn, J. F., Lakhmani, S., Lagoa, C., and Berger, T., "Design of Dynamic Inversion and Explicit Model FollowingControl Laws for Quadrotor UAS," *Journal of the American Helicopter Society*, **65**, 032006 (2020). doi: https://doi.org/10.4050/JAHS.65.032006.

[32]Ferguson, S. W., "A Mathematical Model for Real Time Flight Simulation of Generic Tilt Rotor Aircraft," Technical Report, NASA-CR-166536, 1988.

[33]Garcia Perez, D., Ventura Diaz, P., and Yoon, S., "High-Fidelity Simulations of a Tilt-wing Vehicle for Urban Air Mobility," Proceedings of the AIAA SciTech Forum, National Harbor, MD & Online, January 23–27, 2023. doi: https://doi.org/10.2514/6.2023-2282.

[34]Whiteside, S. K. S., Beau, B. P., Pollard, Antcliff, K. R., Zawodny, N. S., Fei, X., Silva, C., and Medina, G. L., "Design of a Tiltwing Concept Vehicle for Urban Air Mobility," Technical Report, NASA/TM–20210017971, 2021.

[35]Saetti, U., and Rogers, J. D., "Revisited Harmonic Balance Trim Solution Method for Periodically-Forced Flight Vehicles," *Journal of Guidance, Control, and Dynamics*, Vol. 44, (5), May 2021, pp. 1008–1017. doi: https://doi.org/10.2514/1.G005553.

[36]Kokotovic, P. V., O'Malley, R. E., and Sannuti, P., "Singular Perturbations and Order Reduction in Control Theory, an Overview," *Automatica*, Vol. 12, (2), 1976, pp. 123–132. doi: https://doi.org/10.1016/0005-1098(76)90076-5.

[37]Saetti, U., Enciu, J., and Horn, J. F., "Flight Dynamics and Control of an eVTOL Concept Aircraft with a Propeller-Driven Rotor," *Journal of the American Helicopter Society*, **67**, 032012 (2022). doi: https://doi.org/10.4050/JAHS.67.032012.

[38]Saetti, U., and Horn, J. F., "Implementation and Linearization of State-Space Free-Vortex Wake Models for Rotary- and Flapping-Wing Vehicles," *Journal of the American Helicopter Society*, **68**, 042004 (2023). doi: https://doi.org/10.4050/JAHS.68.042004.

[39]Saetti, U., Rogers, J. D., Alam, M., and Jump, M., "Tau Theory-Based Flare Control in Autonomous Helicopter Autorotation," *Aerospace*, **11**, 33 (2024). doi: https://doi.org/10.3390/aerospace11010033.

[40]Saetti, U., Horn, J. F., and Berger, T., "On the Effects of Rotor Induced Vibrational Stability on Helicopter Flight Dynamics," *CEAS Aeronautical Journal,* Vol. 15, 2024, pp. 439–458. doi: https://doi.org/10.1007/s13272-024-00718-w.

[41]Frazzoli, E., Dahlel, M. A., and Feron, E., "Maneuver-Based Motion Planning for Nonlinear Systems With Symmetries," *IEEE Transactions on Robotics*, Vol. 21, (6), December 2005, pp. 1077–1091. doi: https://doi.org/10.1109/TRO.2005.852260.

[42]Berger, T., Tischler, M. B., and Horn, J. F., "High-Speed Rotorcraft Pitch Axis Response Type Investigation," Proceedings of the 77th Annual Forum of the Vertical Flight Society, Virtual, May 10–14, 2021. doi: https://doi.org/10.4050/F-0077-2021-16793.

[43]Sahani, N. A., and Horn, J. F., "Adaptive Model Inversion Control of a Helicopter with Structural Load Limiting," *Journal of Guidance, Control, and Dynamics*, Vol. 29, (2), 2006, pp. 411–420. doi: https://doi.org/10.2514/1.13391.

[44]Theron, J. P., Horn, J. F., Wachspress, D. A., and Enciu, J., "Nonlinear Dynamic Inversion Control for Urban Air Mobility Aircraft with Distributed Electric Propulsion," Proceedings of the 76th Annual Forum of the Vertical Flight Society, Virtual, October 5–8, 2020. doi: https://doi.org/10.4050/F-0076-2020-16396.

[45]Walter, A., Mckay, M., Niemiec, R., Gandhi, F., and Berger, T., "Hover Dynamics and Flight Control of a UAM-Scale Quadcopter With Hybrid RPM and Collective Pitch Control," *Journal of the American Helicopter Society*, Vol. 68, (2), April 2023, pp. 143–160. doi: https://doi.org/10.4050/JAHS.68.022012.

[46]Enciu, J., Horn, J. F., and Langelaan, J. W., "Formation Control of a Rotorcraft Multilift System," *Journal of the American Helicopter Society*, **62**, 042011 (2022). doi: https://doi.org/10.4050/JAHS.62.042011.

[47]Spires, J. M., and Horn, J. F., "Multi-Input Multi-Output Model-Following Control Design Methods for Rotorcraft," *Journal of the American Helicopter Society*, **66**, 032002 (2021). doi: https://doi.org/10.4050/JAHS.66.032002.

[48]Scaramal, M., and Horn, J. F., "Load Alleviation on Compound Rotorcraft Using Load Feedback and Extremum Seeking Control," *Journal of Guidance, Control, and Dynamics*, Vol. 46, (12), 2023, pp. 2399–2408. doi: https://doi.org/10.2514/1.G007192.

[49]Stevens, B. L., and Lewis, F. L., *Aircraft Control and Simulation: Dynamics, Controls Design, and Autonomous Systems, Third Edition*, John Wiley and Sons, Inc., Hoboken, NJ, 2015.

[50]Tischler, M. B., Berger, T., Ivler, C. M., Mansur, M. H., Cheung, K. K., and Soong, J. Y., *Practical Methods for Aircraft and Rotorcraft Flight Control Design: An Optimization-Based Approach*, American Institute of Aeronautics and Astronautics, Reston, VA, 2017.

[51]Blakelock, J. H., *Automatic Control of Aircraft and Missiles*, John Wiley & Sons, New York, NY, 1965. doi: https://doi.org/10.1017/S0001924000057912.

[52]Tischler, M. B., "Frequency-Response Identification of XV-15 Tilt-Rotor Aircraft Dynamics," Ph.D. thesis, Stanford University, Stanford, CA, May 1987.

[53]Padfield, G. D., *Helicopter Flight Dynamics: Including a Treatment of Tiltrotor Aircraft*, 3rd ed., John Wiley & Sons, Hoboken, NJ, 2018.

[54]Meyer, M. A., and Padfield, G. D., "First Steps in the Development of Handling Qualities Criteria for a Civil Tilt Rotor," *Journal of the American Helicopter Society*, Vol. 50, (1), 2017, pp. 33–35. doi: https://doi.org/10.4050/1.3092841.

[55]Saetti, U., and Horn, J. F., "Flight Simulation and Control Using the Julia Language," Proceedings of the AIAA SciTech Forum, San Diego, CA & Virtual, January 3–7, 2022. doi: https://doi.org/10.2514/6.2022-2354.

[56]International, S., "Aerospace Recommended Practice: Stability and Control Design Criteria for Use in Aerospace Vehicle Development," Technical Report SAE AS94900, Society of Automotive Engineers, Stabilization Margins and Control Loop Robustness Guidelines, 1997.

[57]Mansur, M. H., Lusardi, J. A., Tischler, M. B., and Berger, T., "Achieving the Best Compromise between Stability Margins and Disturbance Rejection Performance," Proceedings of the 65th Annual Forum of the Vertical Flight Society, May 27–29, 2022.

[58]Blanken, C. L., Lusardi, J. A., Ivler, C. M., Tischler, M. B., Höfinger, M. T., Decker, W. A., Malpica, C. A., Berger, T., and Tucker, G. E., "An Investigation of Rotorcraft Stability-Phase Margin Requirements in Hover," Proceedings of the 65th Annual Forum of the Vertical Flight Society, Grapevine, TX, May 27–29, 2022.

[59]Berger, T., Ivler, C. M., Berrios, M. G., Tischler, M. B., and Miller, D. G., "Disturbance Rejection Handling Qualities Criteria for Rotorcraft," Proceedings of the 72nd Annual Forum of the Vertical Flight Society, West Palm Beach, FL, May 16–19, 2016.